1-1-2014

Inferring regional sources and sinks of atmospheric CO2 from GOSAT XCO2 data

F Deng
University of Toronto

D Jones
University of Toronto

D Henze
University of Colorado

N Bousserez
University of Colorado

K Bowman
University of California, Los Angeles

See next page for additional authors

Inferring regional sources and sinks of atmospheric CO2 from GOSAT XCO2 data

Abstract

We have examined the utility of retrieved column-averaged, dry-air mole fractions of CO2 (XCO2) from the Greenhouse Gases Observing Satellite (GOSAT) for quantifying monthly, regional flux estimates of CO2, using the GEOS-Chem four-dimensional variational (4D-Var) data assimilation system. We focused on assessing the potential impact of biases in the GOSAT CO2 data on the regional flux estimates. Using different screening and bias correction approaches, we selected three different subsets of the GOSAT XCO2 data for the 4D-Var inversion analyses, and found that the inferred global fluxes were consistent across the three XCO2 inversions. However, the GOSAT observational coverage was a challenge for the regional flux estimates. In the northern extratropics, the inversions were more sensitive to North American fluxes than to European and Asian fluxes due to the lack of observations over Eurasia in winter and over eastern and southern Asia in summer. The regional flux estimates were also sensitive to the treatment of the residual bias in the GOSAT XCO2 data. The largest differences obtained were for temperate North America and temperate South America, for which the largest spread between the inversions was 1.02 and 0.96 Pg C, respectively. In the case of temperate North America, one inversion suggested a strong source, whereas the second and third XCO2 inversions produced a weak and strong sink, respectively. Despite the discrepancies in the regional flux estimates between the three XCO2 inversions, the a posteriori CO2 distributions were in good agreement (with a mean difference between the three inversions of typically less than 0.5 ppm) with independent data from the Total Carbon Column Observing Network (TCCON), the surface flask network, and from the HIAPER Pole-to-Pole Observations (HIPPO) aircraft campaign. The discrepancy in the regional flux estimates from the different inversions, despite the agreement of the global flux estimates suggests the need for additional work to determine the minimum spatial scales at which we can reliably quantify the fluxes using GOSAT XCO2. The fact that the a posteriori CO2 from the different inversions were in good agreement with the independent data although the regional flux estimates differed significantly, suggests that innovative ways of exploiting existing data sets, and possibly additional observations, are needed to better evaluate the inferred regional flux estimates.

Disciplines

Medicine and Health Sciences | Social and Behavioral Sciences

Publication Details

Deng, F., Jones, D. B. A., Henze, D. K., Bousserez, N., Bowman, K. W., Fisher, J. B., Nassar, R., O'Dell, C., Wunch, D., Wennberg, P. O., Kort, E. A., Wofsy, S. C., Blumenstock, T., Deutscher, N. M., Griffith, D. W. T., Hase, F., Heikkinen, P., Sherlock, V., Strong, K., Sussmann, R. & Warneke, T. (2014). Inferring regional sources and sinks of atmospheric CO2 from GOSAT XCO2 data. Atmospheric Chemistry and Physics, 14 (7), 3703-3727.

Authors

F Deng, D Jones, D Henze, N Bousserez, K Bowman, J Fisher, R Nassar, Christopher O'Dell, Debra Wunch, Paul Wennberg, E A. Kort, Steven C. Wofsy, Thomas Blumenstock, Nicholas Deutscher, D W. T Griffith, Frank Hase, Pauli Heikkinen, Vanessa Sherlock, Kimberly Strong, Ralf Sussmann, and Thorsten Warneke

Atmos. Chem. Phys., 14, 3703–3727, 2014
www.atmos-chem-phys.net/14/3703/2014/
doi:10.5194/acp-14-3703-2014

Atmospheric Chemistry and Physics Open Access

Inferring regional sources and sinks of atmospheric CO_2 from GOSAT XCO_2 data

F. Deng[1], D. B. A. Jones[1,2], D. K. Henze[3], N. Bousserez[3], K. W. Bowman[4,2], J. B. Fisher[4], R. Nassar[5], C. O'Dell[6], D. Wunch[7], P. O. Wennberg[7], E. A. Kort[8], S. C. Wofsy[9], T. Blumenstock[10], N. M. Deutscher[11,12], D. W. T. Griffith[12], F. Hase[10], P. Heikkinen[13], V. Sherlock[14], K. Strong[1], R. Sussmann[15], and T. Warneke[11]

[1]Department of Physics, University of Toronto, Toronto, ON, Canada
[2]Joint Institute for Regional Earth System Science and Engineering, University of California, Los Angeles, CA, USA
[3]Department of Mechanical Engineering, University of Colorado, Boulder, CO, USA
[4]Jet Propulsion Laboratory, California Institute of Technology, Pasadena, CA, USA
[5]Climate Research Division, Environment Canada, Toronto, ON, Canada
[6]Department of Atmospheric Science, Colorado State University, Colorado, USA
[7]California Institute of Technology, Pasadena, CA, USA
[8]Department of Atmospheric, Oceanic and Space Sciences, University of Michigan, Ann Arbor, MI, USA
[9]Department of Earth and Planetary Sciences, Harvard University, Cambridge, MA, USA
[10]Karlsruhe Institute of Technology (KIT), Institute for Meteorology and Climate Research (IMK-ASF), Karlsruhe, Germany
[11]Institute of Environmental Physics, University of Bremen, Bremen, Germany
[12]School of Chemistry, University of Wollongong, NSW, Australia
[13]FMI-Arctic Research Center, Sodankylä, Finland
[14]National Institute of Water and Atmospheric Research, Wellington, New Zealand
[15]IMK-IFU, Garmisch-Partenkirchen, Germany

Correspondence to: F. Deng (dengf@atmosp.physics.utoronto.ca)

Received: 31 August 2013 – Published in Atmos. Chem. Phys. Discuss.: 10 October 2013
Revised: 18 February 2014 – Accepted: 24 February 2014 – Published: 11 April 2014

Abstract. We have examined the utility of retrieved column-averaged, dry-air mole fractions of CO_2 (XCO_2) from the Greenhouse Gases Observing Satellite (GOSAT) for quantifying monthly, regional flux estimates of CO_2, using the GEOS-Chem four-dimensional variational (4D-Var) data assimilation system. We focused on assessing the potential impact of biases in the GOSAT CO_2 data on the regional flux estimates. Using different screening and bias correction approaches, we selected three different subsets of the GOSAT XCO_2 data for the 4D-Var inversion analyses, and found that the inferred global fluxes were consistent across the three XCO_2 inversions. However, the GOSAT observational coverage was a challenge for the regional flux estimates. In the northern extratropics, the inversions were more sensitive to North American fluxes than to European and Asian fluxes due to the lack of observations over Eurasia in winter and over eastern and southern Asia in summer. The regional flux estimates were also sensitive to the treatment of the residual bias in the GOSAT XCO_2 data. The largest differences obtained were for temperate North America and temperate South America, for which the largest spread between the inversions was 1.02 and 0.96 Pg C, respectively. In the case of temperate North America, one inversion suggested a strong source, whereas the second and third XCO_2 inversions produced a weak and strong sink, respectively. Despite the discrepancies in the regional flux estimates between the three XCO_2 inversions, the a posteriori CO_2 distributions were in good agreement (with a mean difference between the three inversions of typically less than 0.5 ppm) with independent data from the Total Carbon Column Observing Network (TCCON), the surface flask network, and from the HIAPER Pole-to-Pole Observations (HIPPO) aircraft campaign. The discrepancy in the regional flux estimates from the different inversions, despite the agreement of the global flux estimates

suggests the need for additional work to determine the minimum spatial scales at which we can reliably quantify the fluxes using GOSAT XCO_2. The fact that the a posteriori CO_2 from the different inversions were in good agreement with the independent data although the regional flux estimates differed significantly, suggests that innovative ways of exploiting existing data sets, and possibly additional observations, are needed to better evaluate the inferred regional flux estimates.

1 Introduction

The steady increase of atmospheric CO_2 during the past 200 years is an important contributor to climate change. However, in the past half century only about 45 % of the anthropogenic emissions have remained in the atmosphere (Jones et al., 2005; Canadell et al., 2007), with the remainder absorbed by the oceans and/or fixed by the terrestrial biosphere. Information on the spatial and temporal distribution of the carbon flux is critical to understanding the dominant processes governing the variability of the global carbon cycle, and hence improves our ability to predict future global climate change.

The flask atmospheric CO_2 concentration observations have been one of the most important data sets in quantifying and understanding the global carbon cycle. These data have been intensively used in estimating global and regional carbon sinks and sources via various kinds of atmospheric inversions (e.g., Enting et al., 1995; Fan et al., 1998; Rayner et al., 1999; Gurney et al., 2002; Peylin et al., 2002; Rödenbeck et al., 2003; Law et al., 2003; Patra et al., 2005; Michalak et al., 2005; Baker et al., 2006b; Peters et al., 2007; Deng and Chen, 2011; Bruhwiler et al., 2011). Though there is general agreement in the estimates of hemispheric-scale fluxes, large uncertainties still remain in the estimates of the fluxes on smaller, regional scales, due partly to the limited spatial scale of the observations, errors in the atmospheric models (e.g., Stephens et al., 2007), and to the different configurations of the atmospheric inversions.

Space-based observations of CO_2 provide greater observational coverage than the surface observational network, and several studies (e.g., Park and Prather, 2001; Rayner and O'Brien, 2001; Houweling et al., 2004; Baker et al., 2006a; Chevallier et al., 2007) have suggested that these data will offer greater constraints on estimates of regional sources and sinks of CO_2. Chevallier et al. (2009) conducted an inversion analysis of CO_2 data from the Atmospheric Infrared Sounder (AIRS) and found that it did not improve estimates of the CO_2 fluxes, beyond what they obtained from assimilating data from the surface network. Nassar et al. (2011) showed that observations from the Tropospheric Emission Spectrometer (TES) provide useful additional information on CO_2 sources and sinks, particularly in the tropics, where the density of the surface network is sparse. The additional reduction in uncertainty on estimates of the fluxes obtained by Nassar et al. (2011) was more limited in the extratropics, which could be due to the fact that they used only ocean data between 40° S and 40° N, so the observational coverage was limited. A major challenge with use of the data from space-based thermal infrared instruments such as TES and AIRS is that these instruments were not designed for observing atmospheric CO_2 near the surface, and hence the information content of the CO_2 abundances retrieved from their measurements is limited. Although improved retrievals algorithms may eventually provide better results for the middle and upper troposphere, sensitivity to the lower troposphere will remain elusive.

The Greenhouse Gases Observing Satellite (GOSAT) (Kuze et al., 2009), launched on 23 January 2009, was designed to monitor total atmospheric columns' carbon dioxide (CO_2) and methane (CH_4) globally from space. Recent inversion analyses (Takagi et al., 2011; Maksyutov et al., 2013; Basu et al., 2013) have shown that the total column CO_2 abundances inferred from GOSAT measurements can provide constraints on CO_2 flux estimates that are complementary to those obtained from surface observations. We present here an investigation of the impact of biases in the GOSAT CO_2 data on regional flux estimates of CO_2. We used retrievals of the column-averaged dry-air mole fractions of CO_2 (XCO_2) produced by the NASA Atmospheric CO_2 Observations from Space (ACOS) project for July 2009–December 2010, together with the GEOS-Chem model, to quantify monthly estimates of regional fluxes of CO_2 for 2010. We also employed observations from the surface flask network and compare the fluxes inferred from the flask data with those obtained from the GOSAT XCO_2 data product. The results of the inversion analyses were evaluated using independent data from the Total Carbon Column Observing Network (TCCON) and the HIAPER Pole-to-Pole Observations (HIPPO) project. We also compared our inferred flux estimates in the extratropics with a global flux data set derived from eddy covariance measurements (Jung et al., 2011).

The rest of this article is organized as follows. Section 2 summarizes the retrieval algorithm and data sets used to constrain the model, and to evaluate our modeling results. Section 3 presents the estimated carbon fluxes and the evaluation of performance of the inverse modeling. Regional flux estimates and their sensitivities are discussed in Sect. 4. Conclusions are presented in Sect. 5.

2 Methods and data

2.1 Observations and their uncertainties

2.1.1 Satellite observations

The GOSAT spacecraft (Kuze et al., 2009), launched January 2009, is dedicated to measuring carbon dioxide (CO_2) and

methane (CH_4), using the Thermal and Near-Infrared Sensor for Carbon Observation Fourier Transform Spectrometer (TANSO-FTS). The TANSO-FTS detects gas absorption in the shortwave infrared (SWIR) and thermal infrared (TIR) region of the spectrum. The SWIR consists mainly of reflected solar radiation and, therefore, provides sensitivity to variations in the abundance of CO_2 throughout the troposphere and down into the boundary layer. GOSAT is in a Sun-synchronous polar orbit at an altitude of 666 km, with a repeat cycle of 3 days.

We used here the NASA ACOS GOSAT XCO_2 data product, spanning July 2009 to December 2010. The ACOS retrievals employ an optimal estimation approach to infer atmospheric profile abundances of CO_2, from which the total column dry-air mole fraction (XCO_2) is calculated. The details of the retrieval were described in O'Dell et al. (2012). The retrieved CO_2 profile is given by

$$\hat{\boldsymbol{y}} = \boldsymbol{y}_\mathrm{a} + \mathbf{A}(\boldsymbol{y} - \boldsymbol{y}_\mathrm{a}), \tag{1}$$

where $\boldsymbol{y}$ is the true CO_2 profile (on a 20-level vertical grid), $\boldsymbol{y}_\mathrm{a}$ is the a priori profile used in the retrieval, and $\mathbf{A}$ is the averaging kernel matrix, which gives the sensitivity of the retrieved CO_2 to the true CO_2. From Eq. (1) the XCO_2 can be calculated as

$$\mathrm{XCO_2} = \frac{\int_0^{P_\mathrm{surf}} [\boldsymbol{y}_\mathrm{a} + \mathbf{A}(\boldsymbol{y} - \boldsymbol{y}_\mathrm{a})](1-q)dp}{\int_0^{P_\mathrm{surf}} (1-q)dp}, \tag{2}$$

where q is the water vapor mixing ratio and p is the air pressure. Equation (2) can be written as (Connor et al., 2008)

$$\mathrm{XCO_2} = \mathrm{XCO_2^a} + \sum_j \boldsymbol{h}_j \boldsymbol{a}_{\mathrm{CO_2},j} (\boldsymbol{y} - \boldsymbol{y}_\mathrm{a})_j, \tag{3}$$

where $\boldsymbol{h}_j$ is the contribution of the normalized pressure weighting function for retrieval layer j, $\boldsymbol{a}_{CO_2,j}$ is the normalized column averaging kernel (defined as $\boldsymbol{a}_{\mathrm{CO_2},j} = (\boldsymbol{h}^T\mathbf{A})_j/\boldsymbol{h}_j$), and $\mathrm{XCO_2^a}$ is the a priori CO_2 column assumed by the retrieval ($\mathrm{XCO_2^a} = \boldsymbol{h}^T\boldsymbol{y}_\mathrm{a}$). The pressure weighting function corrects for the presence of water vapor, as described in the denominator of Eq. (2), using the water vapor inferred by the retrieval algorithm.

To assess the impact of residual bias in the XCO_2 retrievals on regional flux estimates, we used versions b2.9 and b2.10 of the ACOS product. ACOS b2.10 is similar to b2.9 version described in O'Dell et al. (2012), with a few important changes: the aerosol scheme was modified to allow more flexibility to deviate from the aerosol prior, the gas absorption models were updated (Thompson et al., 2012), and the prior CO_2 profile was changed to agree with that of TCCON (Wunch et al., 2010). In addition, the filtering and bias correction schemes were refined and updated for version b2.10, and the ACOS b2.10 data used in this study have already been filtered and bias-corrected. We used only the "high-gain" (H-gain) data, which excludes data over bright surfaces, such as deserts, and we neglected the glint observations, that provide coverage over oceans since their biases are not as well quantified. For the b2.9 data, we screened and corrected the bias in the data in the following two ways: (a) we screened out data with retrieved surface pressure (P_surf) that differs from the European Centre for Medium Range Weather Forecasting (ECMWF) surface pressure by more than 5 hPa (Wunch et al., 2011); and (b) we corrected the data using the four-parameter bias correction proposed by Wunch et al. (2011), but with the four coefficients calculated based on the data used in this study. Other than the surface pressure difference mentioned above, we used the same filter criteria according to Wunch et al. (2011) in (a) and (b). The filtered b2.9, filtered and bias-corrected b2.9 and the b2.10 data used here will be referred to as XCO2_A, XCO2_B, and XCO2_C, respectively. Figure 1 shows the zonal mean XCO_2 of four XCO_2 data sets based on different filtering and bias correction approaches. Selecting data with surface pressure errors that are less than 5 hPa reduced the XCO_2 values in the tropics and subtropics in between spring and fall (April–November in the Northern Hemisphere and November–May in the Southern Hemisphere). Application of the Wunch et al. (2011) bias correction (in XCO2_B) further reduced the XCO_2 values in these regions. In contrast, the bias correction in XCO2_B resulted in increases in extratropical XCO_2 in the Northern Hemisphere in winter. XCO_2 values in XCO2_C in general are higher than those in XCO2_A and XCO2_B.

2.1.2 Flask observations

We used here CO_2 mixing ratios measured by a nondispersive infrared absorption technique in air samples collected in glass flasks at NOAA ESRL Carbon Cycle Cooperative Global Air Sampling Network sites (Conway et al., 2011) and Environment Canada (EC) sampling sites. The 72 NOAA sites and 6 EC sites are shown in Fig. 2. The flask measurements are directly traceable to the World Meteorological Organization (WMO) CO_2 mole fraction scale (WMO X2007) (Zhao and Tans, 2006). Measurement accuracy determined from repeated analyses of CO_2 in standard gas cylinders using an absolute manometric technique is ∼0.2 ppm. Measurement precision determined from repeated NDIR analysis of the same air is ∼0.1 ppm. Average agreement between pairs of flasks sampled in series throughout the network is currently ∼0.1 ppm. Therefore, the accuracy and precision of flask measurements are undoubtedly high. When the observations are compared with the model, the model–data mismatches for the observations are larger, since representativeness errors must be accounted for.

The uncertainties assigned to these data for inverse modeling are calculated using the statistics of the differences between the observations and the model simulations of the

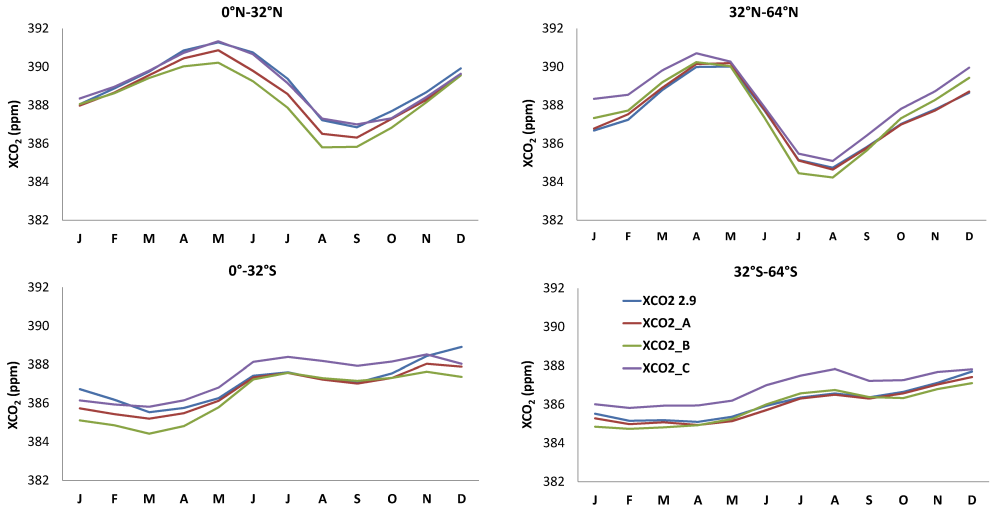

Fig. 1. Monthly mean, zonally averaged XCO_2 data from GOSAT, binned in latitude ranges of 32–64° N, 0–32° N, 32° S–0°, and 64–32° S. Shown are the XCO_2 data (version b2.9) before additional filtering and bias correction (blue lines), and XCO2_A, XCO2_B, and XCO2_C (version b2.10) for the three different bias correction schemes employed.

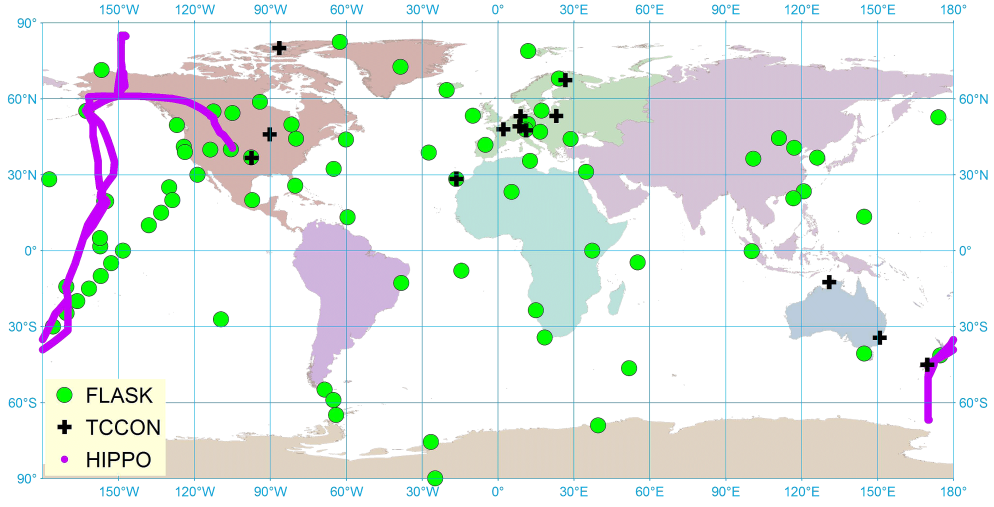

Fig. 2. Global distribution of CO_2 flask sample collection locations from 72 NOAA ESRL Carbon Cycle Cooperative Global Air Sampling Network sites and 6 Environment Canada (EC) sampling sites (green solid symbols), 13 TCCON observatories (black cross symbols), and aircraft sampling locations from the HIPPO-3 campaign (purple dot symbols).

observations using the a priori emissions (Palmer et al., 2003; Heald et al., 2004). We calculated these uncertainties following the procedures detailed by Nassar et al. (2011), and these values were further scaled down to 68 % as the uncertainties used in our inverse modeling.

2.1.3 TCCON observations

We used XCO_2 data from TCCON observatories to evaluate our inferred CO_2 surface fluxes by examining whether the a posteriori CO_2 distribution is in better agreement with the TCCON data. The TCCON sites use ground-based Fourier transform spectrometers to measure high-resolution spectra ($0.02\ cm^{-1}$) in the near infrared ($3800–15\,500\ cm^{-1}$), from which XCO_2 is retrieved. A profile scaling retrieval approach is used to calculate the column CO_2 abundance. The column-averaged dry-air mole fraction is then computed as (Wunch et al., 2011)

$$XCO_2 = 0.2095 \cdot \frac{CO_2^{col}}{O_2^{col}}, \quad (4)$$

where O_2^{col} is the simultaneously retrieved atmospheric oxygen column density, and 0.2095 is the nominal, globally averaged (column-averaged) mole fraction of O_2. TCCON XCO_2 have been rigorously calibrated against the integrated

profiles of CO_2 measured by WMO-standard instrumentation aboard aircraft (Wunch et al., 2010; Washenfelder et al., 2006; Deutscher et al., 2010; Messerschmidt et al., 2011). The TCCON precision and accuracy in the calibrated XCO_2 data are both 0.8 ppm (Wunch et al., 2010).

2.1.4 HIPPO aircraft measurements

The HIAPER Pole-to-Pole Observations (HIPPO) project is a sequence of five global aircraft measurement campaigns that sample the atmosphere from near the North Pole to the coastal waters of Antarctica, from the surface to 14 km (Wofsy et al., 2011). The NCAR/NSF High-performance Instrumented Airborne Platform for Environmental Research (HIAPER), a modified Gulfstream V (GV) jet, hosted the HIPPO campaigns. Major greenhouse gases (CO_2, CH_4, N_2O) and other important trace species were measured at high frequency, with two (or more) independent measurements for each to provide redundancy, check calibration and assess sensor drift. We used the CO_2 field based on 1 s data averaged to 10 s (Wofsy et al., 2012), from two (harmonized) sensors: CO2-QCLS and CO2-OMS. UTC (time), GGLAT (latitude from GPS), GGLON (longitude from GPS), and PSXC (Static pressure) are the fields that we used to match observation with modeled CO_2 mixing ratio. In Sect. 3.2.2, we compared our results with data observed from campaign 3 (HIPPO-3) in March and April 2010, and the route of the campaign is shown in Fig. 2.

2.1.5 Eddy-covariance-based observations

We compared to land–atmosphere CO_2 fluxes from a so-called "upscaled" eddy covariance global product (MPI-BGC; Jung et al., 2009, 2011). This product derives a globally gridded, time-varying data set from in situ measurements of net ecosystem exchange (NEE) at hundreds of flux tower sites worldwide. The towers' instruments (sonic anemometer, infrared gas analyzer) measure fluxes on the order of 1 km, in addition to ancillary measurements (e.g., meteorology) and other fluxes (Baldocchi et al., 2001; Baldocchi, 2008). The MPI-BGC product is derived from a suite of statistical model decision trees that link predictive variables (primarily air temperature, precipitation, and fraction of absorbed photosynthetically active radiation) available at the global scale to the NEE fluxes, and also derives gross primary production (GPP) and total ecosystem respiration (TER) products. The MPI-BGC product can be used only for specific analyses as the world is treated somewhat unrepresentatively like a flux site, e.g., undisturbed, growing, flat, biased towards temperate regions; the mean annual flux, for instance, is not appropriate to compare to. Nonetheless, the MPI-BGC product is valuable for assessing relative spatial distributions, seasonal variability, and timing of min/max uptake, amplitude of the uptake, interannual variability, and hotspots.

2.2 Forward modeling

The GEOS-Chem model (http://geos-chem.org) is used to simulate global atmospheric CO_2. The model is a global 3-D chemical transport model driven by assimilated meteorology from the Goddard Earth Observing System (GEOS-5) of the NASA Global Modeling and Assimilation Office (GMAO). Nassar et al. (2010) described the recent update of the atmospheric CO_2 simulation in GEOS-Chem. In this study, we employed the model at a horizontal resolution of $4° \times 5°$, with 47 vertical layers. Our model simulations include CO_2 fluxes from fossil fuel combustion and cement production, from ocean surface exchange, from terrestrial biosphere assimilation and respiration, and from biomass burning. Specifically, these include (i) monthly national fossil fuel and cement manufacture CO_2 emission from the Carbon Dioxide Information Analysis Center (CDIAC) (Andres et al., 2011); (ii) monthly shipping emissions of CO_2 from the International Comprehensive Ocean–Atmosphere Data Set (ICOADS) (Corbett and Koehler, 2003; Corbett, 2004; Endresen et al., 2004, 2007); (iii) 3-D aviation CO_2 emissions (Kim et al., 2007; Wilkerson et al., 2010; Friedl 1997); (iv) monthly mean biomass burning CO_2 emissions from the Global Fire Emissions Database version 3 (GFEDv3) (van der Werf et al., 2010); (v) biofuel (heating/cooking) CO_2 emission estimated by Yevich and Logan (2003); (vi) the flux of CO_2 across the air–water interface based on the climatology of monthly ocean–atmosphere CO_2 flux by Takahashi et al. (2009); and (vii) 3-hourly terrestrial ecosystem exchange produced by the Boreal Ecosystem Productivity Simulator (BEPS) (Chen et al., 1999), which was driven by NCEP reanalysis data (Kalnay et al., 1996) and remotely sensed leaf area index (LAI) (Deng et al., 2006). The annual terrestrial ecosystem exchange imposed in each grid box is neutral (Deng and Chen, 2011). The emission inventories for 2010 used in our GEOS-Chem simulation are summarized in Table 1.

2.3 Inverse problem and optimizing method

In the inversion analysis, the surface CO_2 sources and sinks ($\boldsymbol{x}$) are related to the atmospheric observations ($\boldsymbol{y}$) by the following relationship

$$\boldsymbol{y} = H(\boldsymbol{x}) + \varepsilon, \tag{5}$$

where H is the forward atmospheric model (such as GEOS-Chem) and $\boldsymbol{\varepsilon}$ is the observation error, or model–data mismatch, which reflects the difference between the observations and the model estimates, including errors associated with observations (instrument errors) and model errors. Considering an a priori estimate of the CO_2 flux $\boldsymbol{x}_\mathbf{a}$, we can

Table 1. Summary of emission inventories of 2010 used in our GEOS-Chem CO_2 model simulation.

Flux type	Inventory data description	2010 global annual flux (Pg C)
Fuel and cement manufacture	Carbon Dioxide Information Analysis Center (CDIAC) $1^\circ \times 1^\circ$ Monthly fossil fuel and cement manufacture CO_2 emissions	8.54
Shipping	Monthly shipping emission of CO_2 from International Comprehensive Ocean–Atmosphere Data Set (ICOADS)	0.19
Aviation	3-D aviation CO_2 emissions based on $2^\circ \times 2.5^\circ$ gridded flight track density.	0.16
Biomass burning	Monthly biomass burning CO_2 emissions available from the Global Fire Emissions Database version 3 (GFEDv3)	1.84
Biofuel burning	Biofuel (heating/cooking) CO_2 emission estimated by Yevich and Logan	0.86
Balanced biosphere	The 3-hourly terrestrial ecosystem exchange produced by BEPS	0.00
Ocean exchange	The climatology of monthly ocean–atmosphere CO_2 flux by Takahashi et al. (2009)	−1.41

construct a cost function

$$J(\boldsymbol{x}) = \frac{1}{2}(H(\boldsymbol{x}) - \boldsymbol{y})^T \mathbf{S}_\mathrm{o}^{-1}(H(\boldsymbol{x}) - \boldsymbol{y}) \quad (6)$$
$$+ \frac{1}{2}(\boldsymbol{x} - \boldsymbol{x}_\mathrm{a})^T \mathbf{S}_\mathrm{a}^{-1}(\boldsymbol{x} - \boldsymbol{x}_\mathrm{a}),$$

where $\boldsymbol{y}$ is a vector of observations and $\mathbf{S}_o$ and $\mathbf{S}_\mathrm{a}$ are the observational and a priori error covariance matrixes, respectively. Minimization of the cost function, subject to the a priori constraint, provides an optimal estimate of the fluxes, based on the available observations.

In the version of GEOS-Chem employed here, we used a 4-dimensional variational (4D-Var) data assimilation system in which we optimize a set of scaling factors to adjust the fluxes in each model grid box to better reproduce the observations over a given time period. The 4D-Var cost function that we minimize is given by

$$J(\boldsymbol{c}) = \frac{1}{2}\sum_{i=1}^{N}(f_i(\boldsymbol{c}) - \boldsymbol{y}_i)^T \mathbf{S}_{\mathrm{o},i}^{-1}(f_i(\boldsymbol{c}) - \boldsymbol{y}_i) \quad (7)$$
$$+ \frac{1}{2}(\boldsymbol{c} - \boldsymbol{c}_\mathrm{a})^T (\mathbf{S}_\mathrm{a}^c)^{-1}(\boldsymbol{c} - \boldsymbol{c}_\mathrm{a}),$$

where N is the number of observations $\boldsymbol{y}_i$ distributed in time over the assimilation window, $\boldsymbol{c}$ is the state vector of scaling factors, and $\boldsymbol{c}_\mathrm{a}$ is the vector of a priori scaling factors, which we typically assume are unity. The a posteriori flux estimate for the jth grid cell is thus given by $\boldsymbol{x}_j = \boldsymbol{c}_j \boldsymbol{x}_{a,j}$. Here the forward model f includes the observation operator that maps the modeled CO_2 profile to the GOSAT XCO_2 observation space

$$\mathrm{XCO}_2^m = f(\boldsymbol{x}) = \mathrm{XCO}_2^\mathrm{a} + \sum_j \boldsymbol{h}_j \boldsymbol{a}_{\mathrm{CO}_2,j}(H(\boldsymbol{x}) - \boldsymbol{y}_\mathrm{a})_j, \quad (8)$$

which is analogous to Eq. (3), with the modeled CO_2 profile $H(\boldsymbol{x})$ interpolated onto the GOSAT retrieval levels. Here $\mathrm{XCO}_2^\mathrm{m}$ is the modeled XCO_2, $\boldsymbol{a}_{\mathrm{CO}_2}$ is the GOSAT column averaging kernel, and $\boldsymbol{h}$ is the pressure weighting function provided with each GOSAT XCO_2 retrieval.

The cost function is minimized iteratively using the L-BFGS algorithm (Liu and Nocedal, 1989) together with the adjoint of GEOS-Chem (Henze et al., 2007). The adjoint provides an efficient way to compute the sensitivity of the model output to inputs and model parameters, and was originally developed and used to optimize aerosol and CO sources (Henze et al., 2007, 2009; Kopacz et al., 2009, 2011; Jiang et al., 2011). In this work, we apply the adjoint to optimize global surface CO_2 sinks and sources.

In constructing the observational error covariance $\mathbf{S}_0$, we used the XCO_2 error estimates provided with the ACOS GOSAT data set. However, these errors were uniformly inflated to ensure that the a posteriori reduced $\chi^2 = 1$ constraint (Tarantola, 2004) was approximately satisfied. This scaling is justified since the observation errors (or the model–data mismatches) incorporate errors associated with observations and the model, which is difficult to characterize. For inversion of the XCO2_A, XCO2_B, and XCO2_C data sets, we inflated the reported ACOS XCO_2 errors by 1.7, 1.57 and 1.175, respectively.

The state vector in the inversion consists of the sum of CO_2 fluxes from fossil fuel combustion and cement manufacture, biofuel burning, biomass burning, exchange with the terrestrial biosphere, and exchange with the ocean. As with the observational error covariance matrix, the a priori uncertainty estimates for these components of $\mathbf{S}_\mathrm{a}$ were adjusted to ensure that the a posteriori reduced $\chi^2 = 1$ constraint was

satisfied and to balance the observational term in the cost function. According to Marland et al. (2008), the uncertainty for estimates of global fossil fuel emissions is about 6 %. However, in constructing $\mathbf{S}_a$, we assigned 16 % for the uncertainty of the fossil fuel emissions in each month and each model grid box. For biomass burning, we started with an assumed uncertainty of 20 %, a global annual uncertainty estimate (van der Werf et al., 2010), which was then inflated to 38 % for emissions in each month and in each model grid box. The annual GPP estimate for 2010 is −119.5 Pg C and we assigned an uncertainty of 22 % of the GPP estimates in each 3 h time step and in each model grid based on global annual uncertainty estimates of 10 to 13 % (Chen et al., 2012). TER, which is the sum of autotrophic and heterotrophic respiration, was specified to be 119.5 Pg C in 2010 since we assumed an annual balanced biosphere. We also assigned 22 % of the prior estimates in each 3 h time step and in each model grid as the prior TER uncertainty. For the ocean flux we assumed an a priori uncertainty of 44 %, to keep the relative proportions for land and ocean in the range of those used in previous studies (Deng and Chen, 2011).

2.4 A posteriori uncertainty estimation

The optimization algorithm requires calculating the gradient of the cost function

$$\nabla J(\boldsymbol{c}) = \sum_{i=1}^{N} \mathbf{K}_i^T \mathbf{S}_{o,i}^{-1}(\mathbf{K}_i \boldsymbol{c}_i - \boldsymbol{y}_i) + (\mathbf{S}_a^c)^{-1}(\boldsymbol{c} - \boldsymbol{c}_a), \tag{9}$$

where $\mathbf{K}_i$ is the Jacobian associated with the linearization of the observation operator (forward atmospheric model) f_i. The second derivative of the cost function is the Hessian,

$$\nabla^2 J(\boldsymbol{c}) = \sum_{i=1}^{N} \mathbf{K}_i^T \mathbf{S}_{o,i}^{-1} \mathbf{K}_i + (\mathbf{S}_a^c)_,^{-1} \tag{10}$$

and for a linear system, such as CO_2 transport, the a posteriori error covariance matrix is given by the inverse of the Hessian,

$$\hat{\mathbf{S}} = \left(\sum_{i=1}^{N} \mathbf{K}_i^T \mathbf{S}_{o,i}^{-1} \mathbf{K}_i + (\mathbf{S}_a^c)^{-1} \right)^{-1}. \tag{11}$$

We approximated the inverse of the Hessian using the Davidon–Fletcher–Powell (DFP) updating formula (Tarantola, 2004). This algorithm starts with an initial approximation of the inverse of the Hessian and combines it with gradient information from recent iterations of the minimization algorithm to update $\hat{\mathbf{S}}$. Since Eq. (7) optimizes the scaling factors but we need $\hat{\mathbf{S}}$ expressed in the flux space, it is necessary to rescale Eq. (9) to express the gradient of the cost function with respect to changes in the fluxes, $dJ/d\boldsymbol{x} = (dJ/d\boldsymbol{c})(d\boldsymbol{c}/d\boldsymbol{x})$, which yields

$$\nabla J(\boldsymbol{x})_j = \nabla J(\boldsymbol{c})_j / (\boldsymbol{x}_a)_j \tag{12}$$

for the gradient of the jth flux element. With this transformation, the update to estimate a posteriori covariance proceeds as follows. Let

$$\delta \boldsymbol{x}_n = \boldsymbol{x}_{n+1} - \boldsymbol{x}_n, \tag{13}$$

$$\delta \nabla J(\boldsymbol{x})_n = \nabla J(\boldsymbol{x})_{n+1} - \nabla J(\boldsymbol{x})_n, \tag{14}$$

and then the inverse of the Hessian can be approximated by DFP updating formula as

$$\hat{\mathbf{S}}_{n+1} = \hat{\mathbf{S}}_n + \frac{\delta \boldsymbol{x}_n \delta \boldsymbol{x}_n^T}{(\delta \nabla J(\boldsymbol{x})_n)^T \delta \boldsymbol{x}_n} - \frac{(\hat{\mathbf{S}}_n \delta \nabla J(\boldsymbol{x})_n)(\hat{\mathbf{S}}_n \delta \nabla J(\boldsymbol{x})_n)^T}{(\delta \nabla J(\boldsymbol{x})_n)^T (\hat{\mathbf{S}}_n \delta \nabla J(\boldsymbol{x})_n)}, \tag{15}$$

where n is the iteration number. The approach used here to estimate the inverse Hessian is similar to that of Muller and Stavrakou (2005). We estimated here the uncertainty on the monthly flux estimates. The large computer memory needed for this approach prohibited us from applying it to estimate annual uncertainties for the regional and global flux estimates.

2.5 Initial condition and model run schemes

The initial fields of the atmospheric CO_2 mixing ratio used are based on the results from an inversion analysis of flask observations from NOAA ESRL Carbon Cycle Cooperative Global Air Sampling Network sites and EC sampling sites. GEOS-Chem was run from 1996 to the end of 2007 without assimilation to obtain a reasonable distribution of CO_2 in the troposphere and stratosphere, and then the flask observations were assimilated from January 2008 to the end of 2009. Comparison of the a posteriori CO_2 field in July 2009 with the GOSAT XCO_2 revealed the assimilated CO_2 fields were biased high relative to the GOSAT v2.9 data. To obtain initial conditions for the XCO_2 inversions, we removed the global mean bias from the a posteriori CO_2 distribution from the flask inversion (hereafter referred to as "the original initial field") at 00:00 GMT on 1 July 2009. We scaled the original initial field by 0.99764 and 0.99734 to match the overall global XCO_2 values for XCO2_A and XCO2_B, respectively, while we directly used the original initial field for XCO2_C. We carried out separate inversions for each of these GOSAT XCO_2 data sets, which are referred to as RUN_A, RUN_B, and RUN_C. For evaluation of the inversion results with independent surface data, we start with the original initial field, rather than the adjusted fields, to simulate the a posteriori atmospheric CO_2. The XCO_2 inversion analyses were conducted from 1 July 2009 to 31 December 2009; however, we report here only the results for 2010 to avoid possible discrepancies in the fluxes due to spin-up during the first 6 months.

3 Results

3.1 Optimized carbon fluxes and their uncertainties

Although our state vector includes emissions of CO_2 from fossil fuel combustion, when we report our a posteriori flux estimates, we remove the a priori fossil fuel estimate from the reported total land flux. Also, although we optimize the GPP and TER fluxes separately, we only report the net ecosystem exchange since the inferred GPP and TER fluxes are highly correlated. Shown in Fig. 3 are annual fluxes for 2010 inferred from the ACOS GOSAT XCO_2 data with the three different screening and correction schemes discussed in Sect. 2.1.1. The global total surface fluxes estimated from the three inversion analyses were similar: -3.79 Pg C, -4.02 Pg C, and -4.35 Pg C for RUN_A, RUN_B, and RUN_C, respectively. Considering the 2.41 ± 0.06 ppm annual mean global carbon dioxide growth rate for 2010 (Conway and Tans, 2012) and the 8.90 Pg C a priori carbon emission from fossil fuel burning (including national fuel combustion and cement manufacturing (8.542 Pg C), international shipping (0.192 Pg C), and aviation (0.162 Pg C)) used for 2010, the global total surface flux should be -3.78 ± 0.13 Pg C ($-3.65 \sim -3.91$ Pg C), using the conversion factor of 2.124 Pg C ppm^{-1} to convert atmospheric CO_2 mixing ratio to Pg C. The estimate from RUN_A is in this range, whereas the estimates from RUN_B and RUN_C exceed the 1-σ lower bound with greater surface carbon uptake of 0.11 and 0.44 Pg C. In terms of the land and ocean breakdown, we estimated that 2.16–2.77 Pg C was fixed by the terrestrial biosphere and that 1.49–1.63 Pg C was absorbed by the ocean in 2010, based on the three inversions. The estimates for the oceanic uptake varied less between the three inversions, which may be due to the fact that the oceanic flux estimates are dominated by the Takahashi et al. (2009) a priori fluxes because we did not use any atmospheric CO_2 observations over the ocean in the three inversions.

As can be seen in Fig. 3, the differences in the spatial distribution of the terrestrial carbon fluxes were large. Significant differences can be found between the inferred CO_2 fluxes from RUN_A and RUN_B, and between those from RUN_A and RUN_C, while the distribution obtained from RUN_B was relatively similar to that obtained from RUN_C. There were large differences, for example, over North America and South America (see Fig. 3). Carbon sources were inferred for the eastern US and southern Mexico from XCO2_A, whereas the eastern US region was found to be a sink, and the source in southern Mexico was much weaker with XCO2_B and XCO2_C data. In South America, the strong carbon source in the eastern region inferred from the XCO2_A data became much weaker when we used XCO2_B and XCO2_ C data sets. Although there were no grid boxes that are strong sources of CO_2 in RUN_C, the annual CO_2 source for tropical South America inferred from

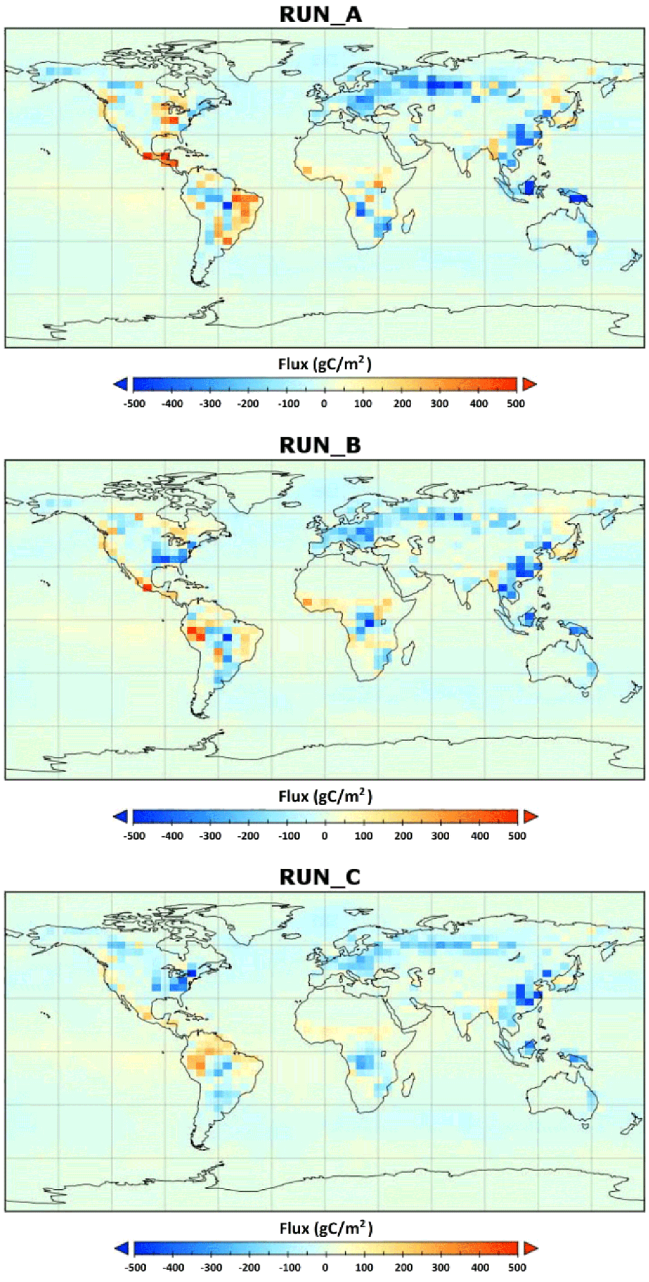

Fig. 3. 2010 annual global surface fluxes of CO_2 in g C m^{-2} from inversion analyses RUN_A, RUN_B, and RUN_C.

XCO2_C data was significantly greater than that inferred from XCO2_A, and XCO2_B data, as the number of inferred source grid cells was greater in RUN_C than in RUN_A and RUN_B.

To help interpret our results, the monthly land fluxes were aggregated into the 11 TransCom land regions (Gurney et al., 2002) that are widely used. The total annual flux and the seasonal variations of the fluxes for each region are shown in Figs. 4 and 5, respectively. We estimated a sink for all four Eurasian regions (Europe, boreal Eurasia, temperate Eurasia,

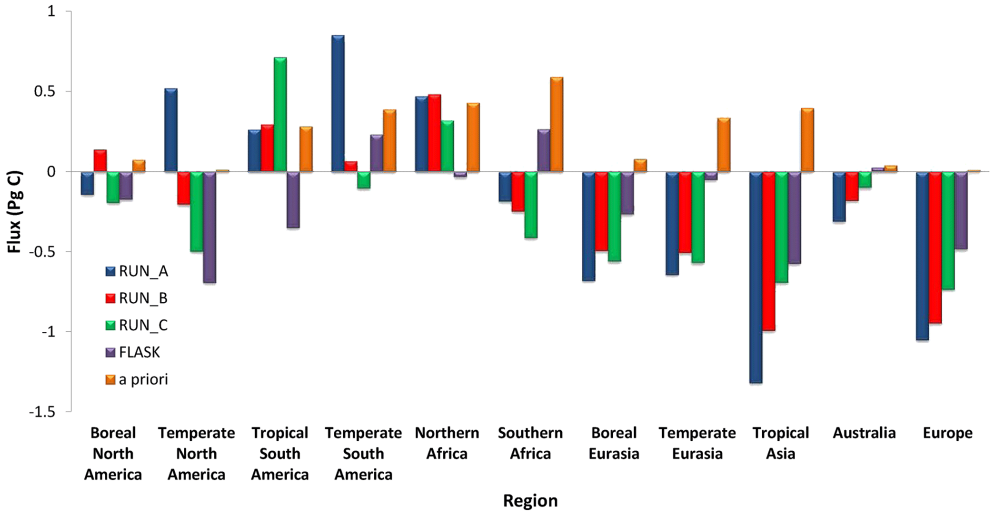

Fig. 4. 2010 annual fluxes for 11 TransCom regions inferred from three XCO_2 data sets, and flask observations. The a priori fluxes (the sum of all prior fluxes excluding emissions from the fossil fuel burning) are also indicated.

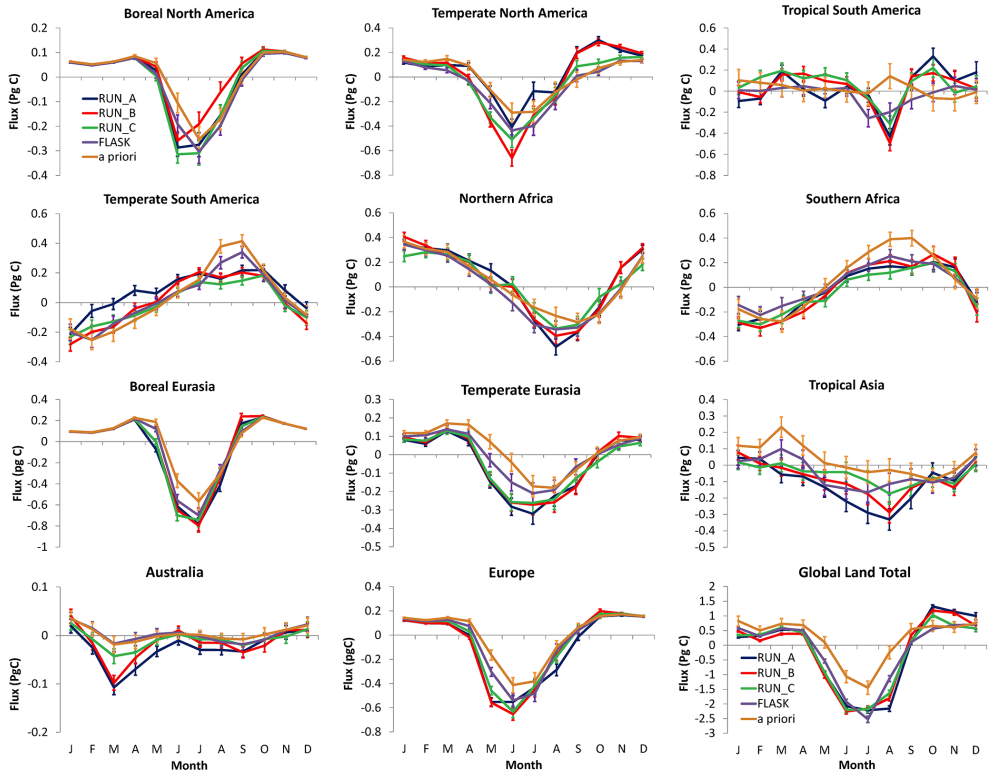

Fig. 5. Monthly fluxes and their uncertainties of 2010 for 11 TransCom regions and global land surface inferred from three XCO_2 data sets (RUN_A (blue), RUN_B (red), and RUN_C (green)), and flask observations (FLASK, purple). The a priori fluxes (the sum of all prior fluxes excluding emissions from the fossil fuel burning) are also indicated (a priori, orange).

and tropical Asia), as shown in Fig. 4, in all three inversion analyses. The estimated aggregated uptake for these regions was 3.69, 2.94, and 2.55 Pg C from RUN_A, RUN_B and RUN_C, respectively. In the extratropics, the estimated fluxes were most similar across the three XCO_2 inversions for boreal Eurasia and temperate Eurasia, for which we estimated an annual CO_2 uptake in the range of 0.49 to 0.68 Pg C and 0.51 to 0.64 Pg C, respectively. Their seasonal variations (Fig. 5) were also similar in the three inversions. We note that the a posteriori fluxes in boreal Eurasia are close to the

a priori used, reflecting, as discussed below, the lack of observational coverage in winter and with observations over the boreal region only available during May through September.

For tropical Asia, the three XCO_2 inversions suggested a sink in the range of 0.69 to 1.32 Pg C. The differences between inversions were manifested mainly in the region around the Indonesian islands (see Fig. 3), and between May to September (see Fig. 5). These differences amounted to an increased uptake of about 0.63 Pg C in the annual regional carbon budget (Fig. 4) in RUN_A compared to RUN_C.

The largest differences in the inferred fluxes for the three XCO_2 inversions were obtained for temperate North America and temperate South America. The differences in the estimated fluxes between RUN_ A and RUN_C were 1.02 and 0.96 Pg C for temperate North American and temperate South American, respectively. The differences in the estimated fluxes between RUN_B and RUN_C were smaller. The fluxes inferred for boreal North America also varied significantly between the three inversions, but the absolute magnitude of the differences was small. We also conducted an inversion analysis of the surface flask data, and the differences between the fluxes inferred from the flask data and those based on the XCO_2 for temperate North American is striking. With XCO2_A we estimated a source of about 0.5 Pg C for temperate North America, whereas with the flask data we estimated a sink of about 0.7 Pg C (Fig. 4). Examination of the seasonal variations in Fig. 5 shown that there were significant differences among the three inversions in the timing and extent of the uptake of CO_2 in July, August, and September in boreal North America. In temperate North America the monthly mean uptake in RUN_A was systematically smaller from May through September than in the other two runs. In temperate South America, CO_2 uptake during the growing season in RUN_A was much less than in the other two runs, especially between January and April. Considering the spatial distribution, these differences in temperate South America were mostly caused by the stronger uptake in RUN_C and RUN_B than in RUN_A in the eastern part of this region.

The posterior errors derived from the 4D-Var inversion using Eq. (15) were aggregated to the TransCom regions. The uncertainties of the land fluxes and the flux for each month are given in Fig. 5. These uncertainties can be further used to calculate the uncertainty reduction percentage (Deng et al., 2007), given as

$$U_r = \left(1 - \frac{\sigma}{\sigma_a}\right) \times 100\,\%, \quad (16)$$

where σ and σ_a are the a posteriori and a priori uncertainties, respectively. The uncertainty reduction obtained for RUN_A is shown in Fig. 6. The uncertainty reduction on the regional flux estimates varied significantly from region to region. The minimum uncertainty reductions can be as small as less than 1 % for the three northern high-latitude regions (boreal North America, Europe, and boreal Eurasia) during winter months, which, as we will discuss below, is due to the scarcity of XCO_2 observations in these regions in winter. The largest uncertainty reduction (exceeding 35 %) for the regional flux estimates was obtained for the fluxes inferred for temperate North America, the two South American regions, and the two African regions. The largest uncertainty reduction that we obtained was about 50 % for tropical South America. We note that these estimates of uncertainty reduction depend largely on our assumed a priori uncertainty. Comparison of the monthly mean fluxes in Fig. 5 indicated that the differences in the flux estimates inferred from the different data sets is larger than the estimated a posteriori uncertainties, suggesting that it is likely that we have underestimated the observation errors. Neglect of spatial and temporal correlations in the a priori error covariance matrix would also result in discrepancies in the predicted a posteriori errors and, consequently, in errors in the estimated uncertainty reduction. Clearly, the estimated uncertainty reduction depends strongly on the specification of the observation and a priori error covariance matrix, which are difficult to characterize. Therefore, in our interpretation of the uncertainty reduction in Sect. 4 we will focus on the relative uncertainty reduction between the different regions and not on the magnitude of the error reduction.

3.2 Evaluation of the inversions

3.2.1 Comparison with GOSAT XCO_2

The objective of the inversion analysis, as described by Eq. (7), was to optimize the fluxes to minimize the mismatch between the model and observations. One way of assessing the success of the inversion is by the degree to which the a posteriori CO_2 matches the observations. Shown in Fig. 7 are the model and GOSAT XCO_2 differences for RUN_A. It shows that the distribution of the model and observation differences was approximately Gaussian. As an indication of the overall inversion performance, the mean global bias was reduced from 2.72 to 0.04 ppm, while the 1-σ spread was also reduced from 2.18 to 1.65 ppm. On the hemispheric scale, the residual bias was smaller in the Northern Hemisphere (NH) than in the Southern Hemisphere (SH). In the NH, the mean bias was 0.01 ppm (reduced from 3.21 ppm in the a priori, with a decrease in the standard deviation from 2.24 to 1.81 ppm), whereas in the SH the mean bias was 0.08 ppm (reduced from 2.02 ppm, with a decrease in the standard deviation from 1.88 to 1.39 ppm). While the mean biases had been reduced satisfactorily in both hemispheres, the larger standard deviation obtained in the NH may reflect the difficulty of reliably capturing the greater biospheric sources and sinks in the NH.

We also examined the seasonality of the residual bias, focusing on April–September as the growing season and October–March as the nongrowing season in the NH, and vice versa for the SH, to broadly reflect the hemispheric biosphere carbon cycle dynamics. During the growing season,

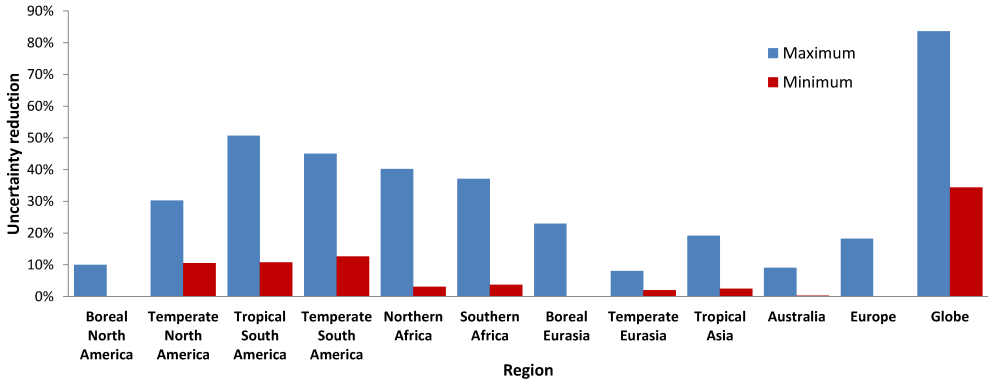

Fig. 6. The maximum and minimum uncertainty reduction on the monthly mean flux estimates aggregated to the TransCom regions. For a given region, the maximum value represents the largest uncertainty reduction obtained for any month in 2010, whereas the minimum value is the smallest uncertainty reduction obtained in any month in 2010.

the residual biases were 0.00 ± 1.89 and 0.03 ± 1.43 ppm for the NH and SH, respectively. During the nongrowing season, the biases were 0.02 ± 1.74 and 0.09 ± 1.37 ppm for the NH and SH, respectively. We believe that the relatively small mean biases of 0.03 and 0.00 ppm obtained for the SH and NH, respectively, during their growing season is due to the fact that more XCO_2 data are available to constrain the inversion analysis during these periods. One common feature among the four cases examined is that the standard deviations of the a posteriori biases were greater during the growing season in both hemispheres than during the nongrowing season, indicating that larger uncertainties may be related to simulating the summertime drawdown of atmospheric CO_2.

3.2.2 Comparison with independent observations

Flask observations

Flask observations provide the research community with highly accurate and precise atmospheric CO_2 measurements that are often used to calibrate new atmospheric CO_2 measurements. We used here flask observations from the 78 observing sites shown in Fig. 2, corresponding to 3016 flask observations in 2010, to evaluate the a posteriori CO_2 fluxes. We sampled the modeled CO_2 distribution at the appropriate measurement location and time (to within half an hour of the measurement time). Using the a posteriori results from the three GOSAT XCO_2 inversions, we estimated a mean difference of -0.88, -0.99, and 0.01 ppm relative to the 3016 flask observations in 2010. These mean differences for RUN_A and RUN_B could be due to the overall systematic errors transferred from the XCO_2 data when we adjusted the initial CO_2 distribution in the inversion to remove the mean mismatch with the GOSAT data. Therefore, it would be inappropriate to directly compare the modeled a posteriori mixing ratios against real flask observations to evaluate our flux estimates. Instead we simulated the a posteriori CO_2 mixing ratios, based on the optimal CO_2 flux estimates, starting from the original initial CO_2 field (which, as discussed in Sect. 2.5, was based on an assimilation of the surface data).

Figure 8 shows the observed and simulated CO_2 time series at four flask sites: ALT (Alert, Nunavut, Canada), MLO (Mauna Loa, Hawaii, USA), GMI (Mariana Islands, Guam), and CGO (Cape Grim, Tasmania, Australia). Because we assumed a balanced biosphere (with zero annual net uptake) for our a priori fluxes, the a priori CO_2 distribution significantly overestimates the observations at the flask sites by the end of 2010. The a priori overestimate largely reflects the well-established secular increase in atmospheric CO_2 due to anthropogenic emissions, and the inversion successfully corrects for it. In general, the seasonal variation of the observed atmospheric CO_2 time series has been satisfactorily simulated using the a posteriori fluxes, optimized from ACOS GOSAT XCO_2 data, considering the spatial and temporal resolution of the model. We started with a neutralized annual a priori flux to better assess the ability of the observations to constrain the flux estimates. The mean, the standard deviation (SD), and the mean absolute value (MAV) of the mismatch between the a posteriori model and observations are listed in Table 2. For ALT, MLO, and GMI, the mean differences were small, much less than 1 ppm. For CGO, however, the a posteriori CO_2 was biased low by slightly more than 1 ppm for RUN_A and RUN_B, while the bias was significantly reduced to -0.68 for RUN_C. For all 78 flask sites, the mean of the model–observation mismatch was 0.02, 0.05, and 0.01 ppm for RUN_A, RUN_B, and RUN_C, respectively, indicating that, on average, the observations had been simulated well with the optimal fluxes. The underestimate at CGO is not unique to that station. We found that the a posteriori fluxes underestimate CO_2 at the surface sites across the southern extratropics. However, the magnitude of the underestimate was highly variable. At Palmer Station, Antarctica (PSA), for example, the mean difference was only -0.21 ppm and the MAV was 0.21 (not shown) in RUN_A, compared to -1.18 ppm for the mean difference and 1.18 for

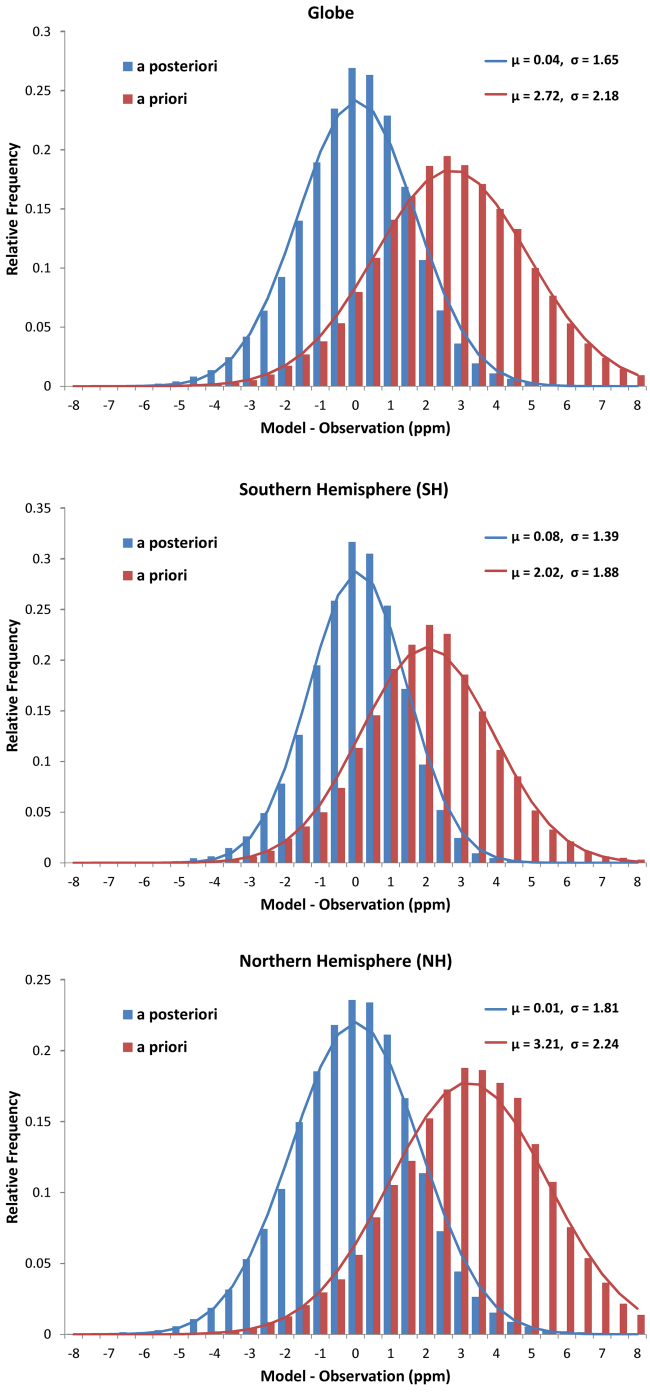

Fig. 7. The distribution of the modeled minus observed XCO_2 in ppm. The red bars are from the modeled a priori XCO_2 minus the observed XCO_2, whereas the blue bars are from the modeled a posteriori XCO_2 minus the observed XCO_2. The blue and red solid lines show a normal distribution for the a priori and a posteriori differences. The distribution means and the standard deviations are indicated.

the MAV at CGO. Examination of the mean and MAV suggests that RUN_C provides a relatively better overall simulation compared with observations from all 78 sites.

TCCON observations

We evaluated the a posteriori flux estimates using TCCON by comparing the observations with the a posteriori atmospheric CO_2 mixing ratios that were produced with the model simulation initialized with the original initial CO_2 field. As with the flask data, the model was sampled at the observation location and time (to within half an hour). To compare with the TCCON XCO_2, the modeled CO_2 concentrations were mapped to the TCCON 71 vertical layers and then transformed using the a priori profile and averaging kernel extracted from the TCCON data set. Finally, the XCO_2 values were calculated using the approach of Wunch et al. (2011). Fig. 9 shows the observed and modeled XCO_2 time series at four selected sites: (1) Lamont, USA; (2) Sodankylä, Finland; (3) Izana, Tenerife; and (4) Wollongong, Australia. The a posteriori CO_2 field reproduced well the observed seasonal variations at these four sites. However, the model underestimated the XCO_2 at Lamont and Izana in summer (between days 150 and 250), and overestimated it at Sodankylä and Wollongong throughout 2010. Using the scaled initial field, our calculation shows that the means of the mismatches between the modeled a posteriori hourly atmospheric CO_2 mixing ratios and the observations at 13 TCCON sites in 2010 are −0.79, −1.27, and 0.06 ppm for all three inversions, respectively.

The mean model and observation mismatch, the SD, and the MAV of the differences for all 13 TCCON sites are given in Table 3. The mean mismatch for all 13 sites was 0.16, −0.23, and −0.06 ppm for RUN_A, RUN_B, and RUN_C, respectively. On average, as indicated in Table 3, the XCO_2 at Park Falls, Orleans, Karlsruhe, Bialystok, Darwin, and Lauder were well simulated by the a posteriori fluxes from all three inversions, with mean biases that are less than or equal to 0.70 ppm. RUN_B produced the best a posteriori CO_2 compared to the TCCON observations in the Southern Hemisphere (including Darwin, Wollongong, and Lauder) in terms of both the mean and the MAV, while RUN_A produced the best a posteriori CO_2 comparing with northern subtropical (Lamont and Izana) observations. For the northern sites, no single inversion consistently agreed well with all the observations; however, RUN_B and RUN_C generally produced better a posteriori CO_2 fields relative to the observations. Considering all 13 sites, RUN_C had the least absolute mean bias (0.06 ppm) and the least MAV (0.91 ppm). It also had the strongest correlation ($r^2 = 0.80$) with the observed XCO_2 at all 13 sites. It should be noted that the number of TCCON observations at each of the 13 sites affects the statistics for all 13 sites, and therefore the statistics for all 13 sites should be interpreted with caution.

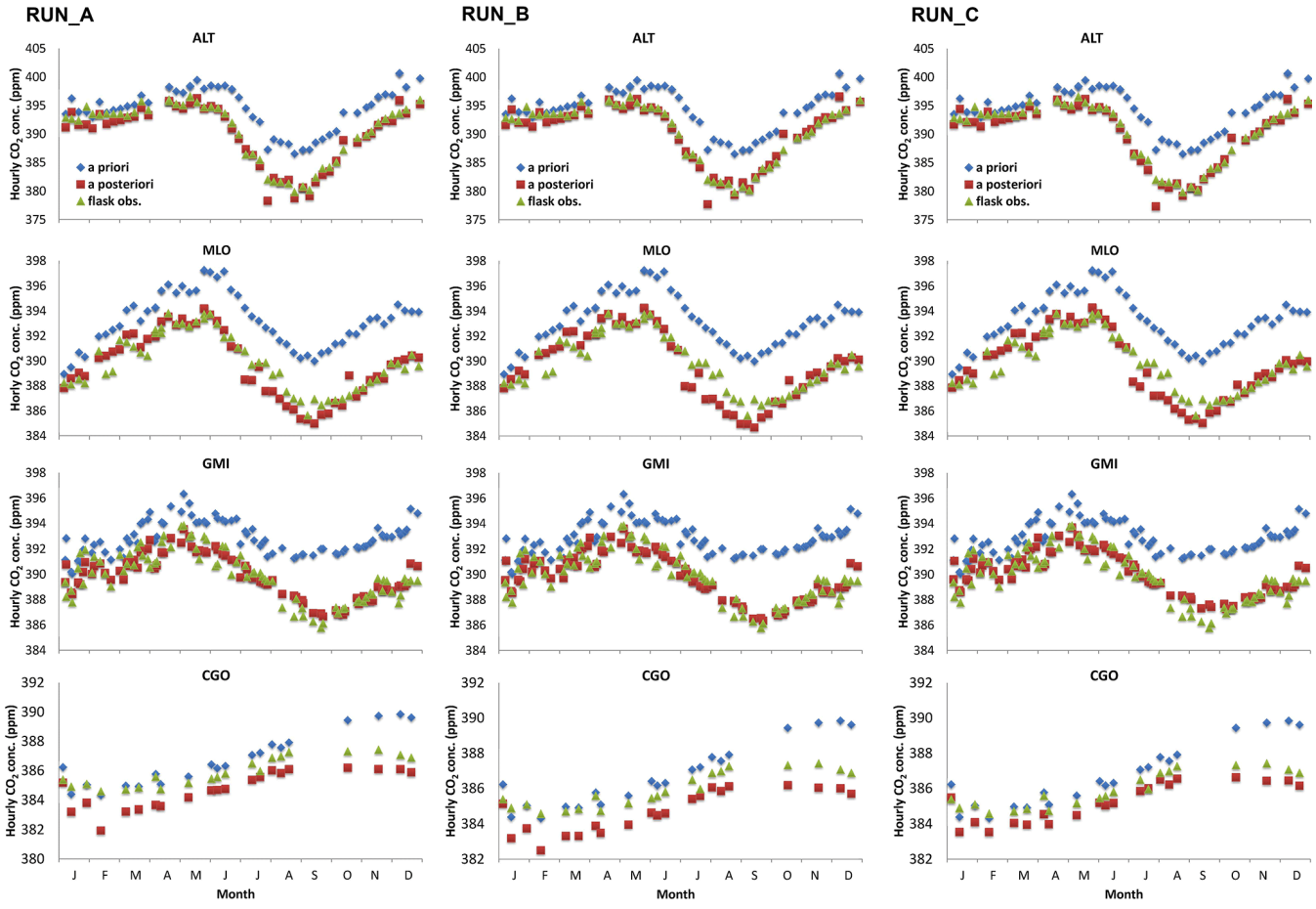

Fig. 8. The a priori (blue diamonds) and a posteriori (red squares) model estimates, and real flask observations (green triangles) of 2010 for 4 selected sites for RUN_A, RUN_B, and RUN_C. These a priori and a posteriori simulations use the original initial field, which differs from those used for the inverse modeling.

Table 2. The mean, standard deviation (SD), and the mean absolute value (MAV) of the a posteriori model–observation mismatch in 2010 for the four flask sites listed in Fig. 8, and for the global average of the 78 flask sites shown in Fig. 2. These a posteriori simulations use the original initial field, which differs from those used for the inverse modeling in RUN_A and RUN_B.

Site code (lat/lon)	RUN_A			RUN_B			RUN_C		
	mean	SD	MAV	mean	SD	MAV	mean	SD	MAV
ALT (82.5° N / 62.5° W)	−0.52	1.08	0.91	-0.17	1.23	0.87	−0.42	1.14	0.83
MLO (19.5° N / 155.6° W)*	−0.14	0.92	0.72	−0.16	1.12	0.85	−0.11	0.99	0.75
GMI (13.4° N / 144.8° E)	−0.04	0.89	0.70	−0.07	0.88	0.69	0.11	0.91	0.70
CGO (40.7° S / 144.7° E)	−1.18	0.51	1.18	−1.19	0.41	1.19	−0.68	0.35	0.69
78 sites	0.07	5.32	2.67	0.05	5.47	2.74	0.01	5.36	2.62

* MLO observatory is at an altitude of 3397 m and is probably not resolved well in our posterior simulations (Nassar et al., 2010).

HIPPO aircraft measurements

As discussed in Sect. 2.1.4, we compared our a posteriori CO_2 fields with the 10 s averaged HIPPO-3 data. At this temporal resolution, the HIPPO data reflect CO_2 on spatial scales smaller than the model resolution. We did not average the HIPPO data onto the model grid, so the differences between the model and the observations also reflect representativeness errors associated with the coarse model grid. Listed in Table 4 are the mean differences, the standard deviation, and the mean absolute value of model and observation mismatch for all 24 303 HIPPO-3 observations. In general, the results from the three inversions were not significantly different from each

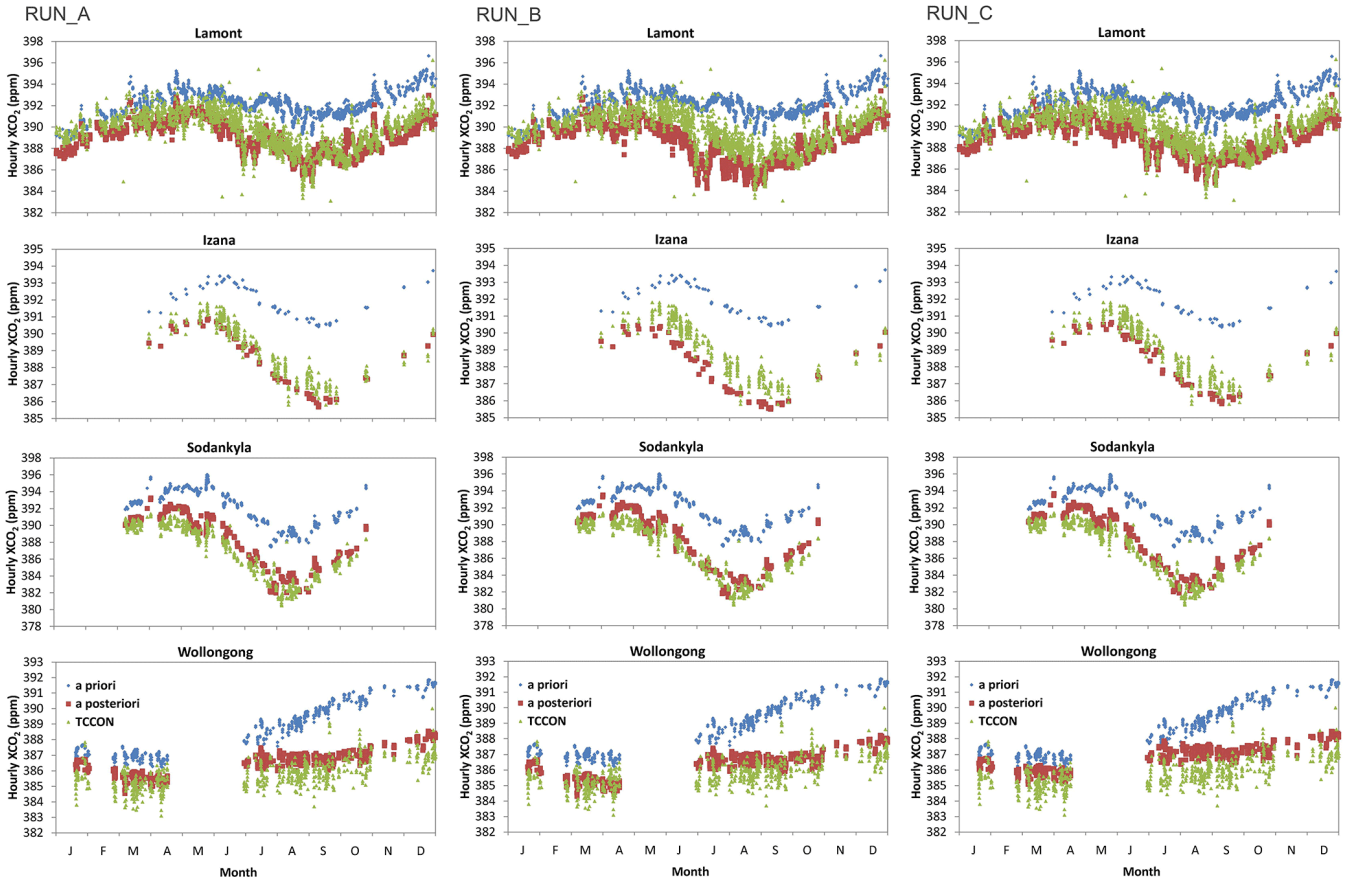

Fig. 9. The TCCON XCO_2 (green) of 2010 for four selected sites and the a priori (blue) and a posteriori (red) XCO_2 for RUN_A, RUN_B, and RUN_C. The a priori and a posteriori simulations used the original initial CO_2 field that was not scaled to remove the global offset relative to the GOSAT XCO_2.

other. We estimated mean differences of −0.07, −0.08, and −0.17 ppm for RUN_A, RUN_B, and RUN_C, respectively. In contrast, using the scaled initial field resulted in mean differences between the a posteriori CO_2 and the HIPPO data of −1.01, −1.12, and −0.17 ppm, respectively, reflecting the global mean bias in the initial conditions used for the XCO_2 inversions.

To better evaluate the performance of the inversion analyses, we also compared the a posteriori CO_2 to the HIPPO data only between 1000 m and 5000 m in altitude. Figure 10 shows three sets of plots comparing simulated HIPPO observations with optimal surface fluxes from our three inversions with the HIPPO-3 observations. As our model was sampled with a temporal resolution of one hour, and the spatial resolution of the model is coarse (4° × 5°), the modeled CO_2 did not reproduce much of the detailed structure seen in the observations. The a posteriori simulations based on the optimal fluxes from RUN_B deviated from the observation the most in the southern high latitudes. For example, the mean differences in the southern high latitudes, 70° S–45° S, were as large as −0.92 ppm. However, the simulations based on a posteriori fluxes from RUN_B were less biased relative to the observations in the tropics and the Northern Hemisphere. The a posteriori simulation based on RUN_C had the smallest bias in the Southern Hemisphere between 15° S to 70° S, but the largest bias in the tropics (15° S to 15° N). The posterior CO_2 from RUN_A deviated from the observations the most in the Northern Hemisphere (15° N to 80° N). Overall, the simulations compared well to the HIPPO data. The correlation between the a posteriori simulations and the observations were $r^2 = 0.96$ for all three inversion runs.

Eddy covariance-derived product

In Fig. 11 we compared our inferred fluxes for temperate North America and Europe with the MPI-BGC fluxes (Jung et al., 2011), which are empirically derived from eddy covariance measurements. We focused on North America and Europe for this comparison since the density of eddy covariance towers is greatest in these regions. For temperate North America, the MPI-BGC fluxes suggest weaker uptake in May and June than inferred from RUN_B, whereas the June MPI-BGC flux is in agreement with the estimates in RUN_A and

Table 3. The mean difference, standard deviation (SD), and the mean absolute value (MAV) of the model–observation mismatch for 13 TCCON sites in 2010. Also listed are the averages and correlation for all 13 sites. These a posteriori simulations use the original initial field, which differs from those used for the inverse modeling in RUN_A and RUN_B.

Site (lat/lon)	RUN_A			RUN_B			RUN_C		
	mean	SD	MAV	mean	SD	MAV	mean	SD	MAV
Lamont (36.6° N, 97.5° W)	−0.48	1.03	0.89	−1.05	1.15	1.24	−0.72	0.95	0.92
Park Falls (45.9° N, 90.3° W)	−0.29	0.96	0.81	−0.31	0.92	0.77	−0.29	0.82	0.69
Eureka (80.1° N, 86.4° W)	1.10	1.05	1.25	0.93	0.89	1.04	0.94	0.95	1.08
Izana (28.3° N, 16.5° W)*	−0.46	0.49	0.55	−1.12	0.61	1.15	−0.68	0.51	0.74
Orleans (47.97° N, 2.11° E)	−0.41	0.88	0.79	−0.55	0.77	0.78	−0.26	0.84	0.70
Karlsruhe (49.1° N, 8.43° E)	0.62	1.25	1.04	−0.28	1.05	0.82	0.16	1.00	0.73
Bremen (53.1° N, 8.85° E)	−0.82	1.02	1.08	−1.16	1.34	1.40	−0.97	1.29	1.27
Garmisch (47.5° N, 11.1° E)	1.16	1.47	1.47	0.48	1.02	0.88	0.67	1.02	0.96
Bialystok (53.2° N, 23.0° E)	0.66	1.27	1.08	0.20	1.39	1.03	0.60	1.18	1.02
Sodankylä (67.4° N, 26.6° E)	1.11	0.86	1.22	0.99	0.92	1.17	1.15	0.85	1.27
Darwin (12.4° S, 130.9° E)	0.11	0.52	0.41	0.07	0.50	0.39	0.65	0.43	0.69
Wollongong(34.4° S, 150.9° E)	0.81	0.65	0.91	0.61	0.68	0.79	1.09	0.65	1.15
Lauder (45.0° S, 169.7° E)	0.18	0.76	0.60	0.03	0.74	0.57	0.48	0.74	0.70
All 13 sites	0.16	1.22	0.95	−0.23	1.24	0.98	0.06	1.15	0.91
r^2	0.77			0.76			0.80		

* Izana is at an altitude of 2370 m and is probably not resolved well in our posterior simulations.

Table 4. The mean difference, standard deviation (SD), and the mean absolute value (MAV) of the model–observation mismatch for HIPPO-3 observations.

	Mean	SD	MAV
RUN_A	−0.07	1.37	1.02
RUN_B	−0.08	1.39	1.05
RUN_C	−0.17	1.33	0.97

RUN_C. However, for July–September the MPI-BGC data product suggests greater uptake than the three XCO_2 inversions and the flask inversion. For Europe, the MPI-BGC data are generally consistent with the results of the inversions. The major discrepancy between the three XCO_2 inversions and the MPI-BGC data occurs in May, when all three inversions suggested greater uptake of CO_2. In contrast, the flask inversion suggested slightly weaker uptake. Wintertime fluxes in the inversions tend to be larger sources than that from MPI-BGC in Europe.

4 Discussion

4.1 Regional flux estimates

Terrestrial ecosystem (biosphere) models often underestimate the seasonal amplitude of CO_2 in the Northern Hemisphere (Randerson et al., 2009), and inversion analyses that employ these terrestrial ecosystem models to provide a priori flux estimates underestimate the CO_2 seasonal amplitude by 1 to 2 ppm (Basu et al., 2011; Peters et al., 2010). In this study, we used the annual balanced, 3-hourly terrestrial ecosystem fluxes as described by Deng and Chen (2011), which also produced a weak seasonal cycle in the a priori CO_2 fields. However, as shown in Figs. 8 and 9, the a posteriori simulations reproduced well the amplitude of the seasonal cycle measured at the flask and TCCON sites. This improvement in the modeled seasonal cycle could be attributed to the good spatial coverage of the GOSAT observations during the growing season. This correction in the modeled seasonal cycle is reflected in the significantly greater uptake of CO_2 during the growing season obtained for the regions in the extratropical Northern Hemisphere (Fig. 5).

Using the ACOS XCO_2 data screened and bias-corrected by the three different approaches produced significantly different surface fluxes for regions such as boreal North America, temperate North America, and temperate South America. The sensitivity of the inferred flux estimates for boreal North America is not surprising since the GOSAT observational coverage is limited at high latitudes over North America. The temperate North America region has been described as a sink in previous inversions using flask observations of atmosphere CO_2 (Deng and Chen, 2011; Gurney et al., 2004; Peters et al., 2007; Rayner et al., 2008; Deng et al., 2007). Here we estimated the region to be a significant source in RUN_A, but a weak sink in RUN_B and a strong sink in RUN_C. Our flask inversion suggested a stronger sink for the region. The differences are mostly caused by the uptake in the growing season. All three XCO_2 inversions and the flask inversion estimated peak uptake of CO_2 in temperate North

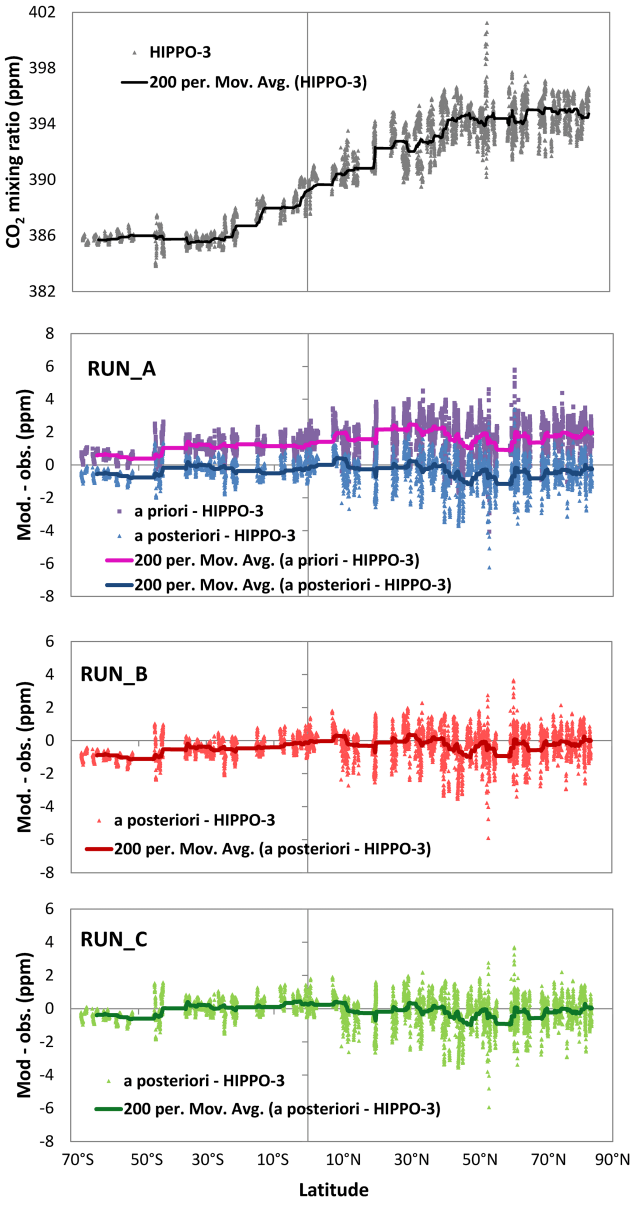

Fig. 10. Comparison of modeled a priori and a posteriori CO_2 mixing ratios with HIPPO observations from 70° S to 84° N and 1000 to 5000 m. Top panel is the HIPPO observations (grey) and their moving average; modeled atmospheric CO_2 based on prior fluxes (purple), posterior fluxes from RUN_A (blue), posterior fluxes from RUN_B (red), and posterior fluxes from RUN_C (green) deviated from HIPPO observations, and their moving averages are plotted in the remaining three panels. The a priori and a posteriori simulations use the original initial CO_2 field that was not adjusted to remove the global bias relative to the GOSAT XCO_2 data.

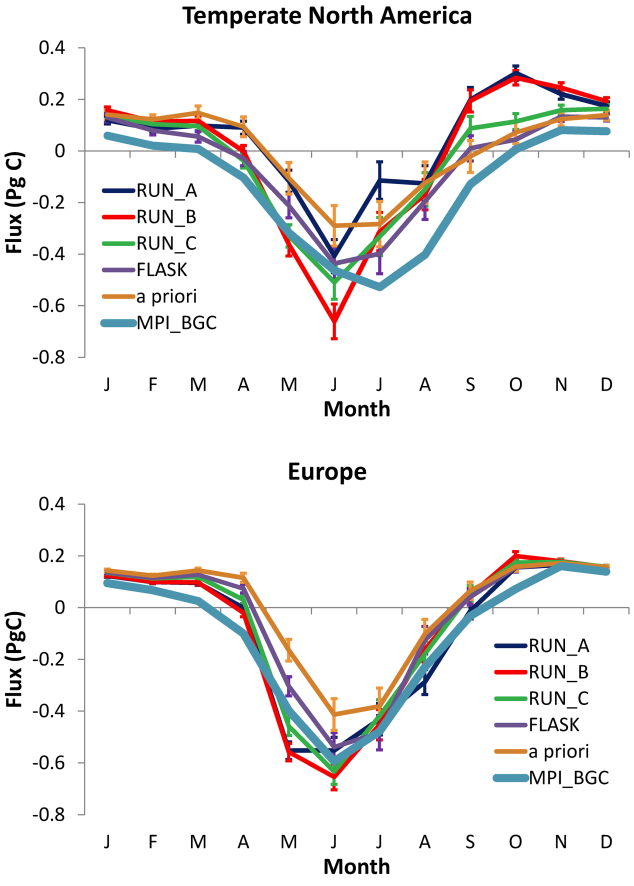

Fig. 11. Monthly fluxes and their uncertainties of 2010, as in Fig. 5, for temperate North America and Europe. Shown are the fluxes inferred from the three XCO_2 data sets (RUN_A, RUN_B, and RUN_C), and the flask observations (FLASK). Also plotted are the flux estimates from the MPI-BGC flux data product. The a priori fluxes (the sum of all prior fluxes excluding emissions from the fossil fuel burning) are also indicated (a priori).

America in June, with the flask and RUN_A inversions producing similar estimates of the June uptake. In contrast, in RUN_B and RUN_C, we estimated stronger uptake in June. Unlike the flask inversion, all the XCO_2 inversions produced much weaker uptake in July compared to June. Comparison with the TCCON observations at Lamont from day 120 to 250 (Fig. 9) shows the strong negative bias for RUN_B and RUN_C, which could indicate that the stronger uptake inferred in these inversions for temperate North America represent an overestimate of the actual sink during the growing season (in the absence of compensatory changes in the flux from other regions). Surface flask observations – for example, at the KEY site and inland at NWR and SGP (not shown) – also suggest that the summertime sinks estimated in RUN_B and RUN_C for temperate North America were overestimated. A weak sink for temperate North America is possible for 2010 as a result of the cold spring and hot and dry summer in the southeast US during 2010 (Blunden et al., 2011). In addition, fire emissions in southern British Columbia, Canada, in July would have further reduced the net uptake of CO_2 from temperate North America in 2010. Indeed, these could be responsible for the strong decrease in uptake in the three XCO_2 inversions in July.

For temperate South America, we estimated a strong source in RUN_A, a weak source in RUN_B, and a strong sink in RUN_C (Fig. 4). As shown in Fig. 5, these differences are largely due to the estimated uptake during January to May. For these months, RUN_B and RUN_C suggest greater uptake than RUN_A, with sink estimates comparable to those inferred from the flask data and similar to the a priori fluxes. Comparison with the flask data from the PSA flask station at the South Pole (not shown) reveals that the a posteriori CO_2 concentrations from all three XCO_2 inversions underestimate the observed CO_2 concentrations, with the underestimate being greater for RUN_B during the first half of 2010. However, this is not the case for RUN_C though the inferred fluxes from XCO2_C are almost identical to those from XCO2_B for the same period. A possible explanation is that lower uptake in Australia, inferred from XCO2_C, could in part compensate for the inferred fluxes from temperate South America. Comparison with the HIPPO-3 data (see Fig. 10) shows that the a posteriori CO_2 fields from RUN_B are also more negatively biased relative to the independent aircraft data than those from RUN_A and RUN_C, suggesting the need for a weaker uptake or large emissions of CO_2 in the southern extratropics in early 2010.

4.2 Regional sensitivity analysis

The uncertainty reductions on the regional flux estimates, as shown in Fig. 6, vary considerably both in space (regions) and time (seasons). The largest uncertainty reduction (about 50 %) was for the flux estimates from tropical South America. The other regions with large uncertainty reduction are temperate South America, northern and southern Africa, and temperate North America. The large uncertainty reduction on the flux estimates in the tropics is not surprising given the observational coverage of GOSAT. We note here that interpretation of the uncertainty reduction should be taken with care, as it depends on the magnitude of the assumed a priori uncertainty and observation errors. Furthermore, we used a scheme in which the a priori uncertainties were proportional to the a priori flux estimates, so regions with large absolute a priori fluxes (such as tropical South America) would have large a priori uncertainties and, consequently, large uncertainty reductions, whereas regions with small absolute a priori fluxes could have small uncertainty reductions. Therefore, the uncertainty reductions should be used only as a metric to assess the relative impact of the observation constraints on the regional flux estimates.

In the northern extratropics, the largest uncertainty reduction obtained was for temperate North America. Examination of the uncertainty reduction of the monthly mean fluxes in 2010 revealed that the uncertainty reduction in the flux estimate for temperate North America was at a maximum (about 35 %) in April, with comparably large uncertainty reduction in October. The smallest uncertainty reduction was for December 2010, due to the smaller number of observations used for quantifying the December fluxes compared to previous months (since the assimilation period ended on 31 December 2010). The other extratropical regions with large uncertainty reduction are Europe and boreal Eurasia. For both regions the uncertainty reduction on the flux estimates was small in winter and peaked at about 20 and 25 % in May and July, respectively.

To explain the relative differences in the uncertainty reduction for Europe and North America, for example, we constructed the regional Jacobians, which give the sensitivity of the modeled XCO_2 to the regional flux estimates. The Jacobian is obtained by taking the derivative of the observation operator Eq. (8) with respect to the emissions, which gives

$$\frac{d\mathrm{XCO}_2^m}{d\boldsymbol{x}} = \sum_j \boldsymbol{h}_j \boldsymbol{a}_{\mathrm{CO}_2,j} \left(\frac{dH(\boldsymbol{x})}{d\boldsymbol{x}}\right)_j . \quad (17)$$

The derivative $dH(x)/dx$ is available from the adjoint sensitivities, but we choose here to estimate them using separate tracers for each of the main continental regions in the northern extratropics. With this construction of the sensitivities it will be easier to interpret our results in the context of previously published TransCom inversions. We specify a 1 Pg C source for North America, Europe, and Asia, using the distribution of CO_2 fluxes shown in Fig. 12. This 1 Pg C source of CO_2 was emitted over a period of one month for each region, but the resulting tracer distribution was simulated for three months. The sensitivities were calculated using Eq. (17), by sampling the tracer distribution at the GOSAT observation locations and time (to within an hour) and applying the GOSAT averaging kernels. The sensitivities for January 2010 XCO_2 to fluxes in January are shown in Fig. 13. Over Europe there is weak sensitivity to European fluxes due to the limited observational coverage. In contrast, there is greater sensitivity to North American emissions due to the good coverage over the United States. This accounts for the greater wintertime uncertainty reduction in flux estimates from North America than from those from Europe. In April, there is significantly greater observational coverage over Europe, and as a result (Fig. 13) there is strong sensitivity of the April XCO_2 over Eurasia to European fluxes in April. In May, as a result of transport, the sensitivities of the modeled XCO_2 to April fluxes have been reduced relative to the sensitivities in April (Fig. 14). We find that European and North American fluxes in April most strongly influence XCO_2 values across Eurasia in May. The sensitivity of the Eurasian XCO_2 to North American fluxes is due to the efficient transport of air from the North American boundary layer across the Atlantic to Europe in the free troposphere and in the boundary layer (Li et al., 2002).

To help interpret the regional sensitivities, we calculated the transit times of air from the boundary layer of North America, Europe, and Asia to the receptor regions shown in Fig. 12. Instead of emitting the CO_2 for the regional tracers over a period of one month, we emitted the 1 Pg C from

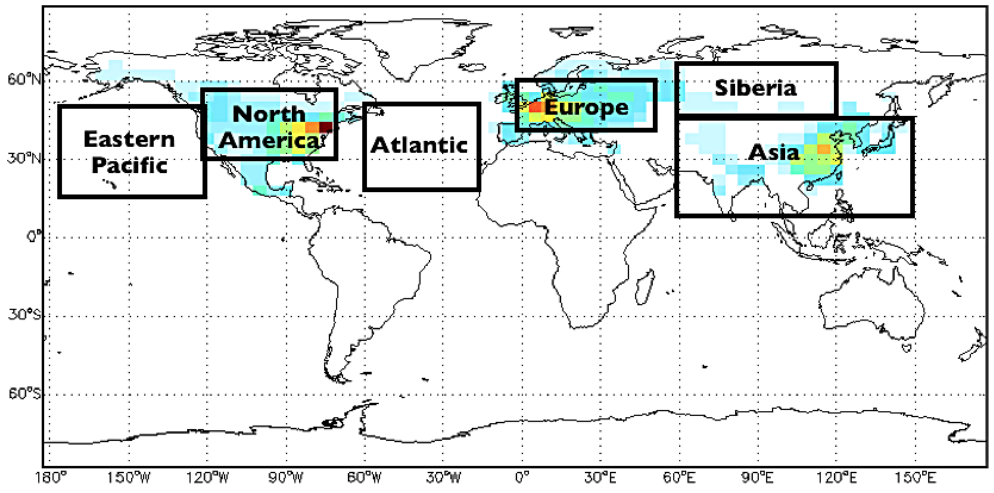

Fig. 12. Distribution of CO_2 fluxes in North America, Europe, and Asia used for the pulse experiment to simulate the sensitivities of the modeled XCO_2 to the regional fluxes, using Eq. (17). The flux pattern represents the combined influence of the fluxes from the biosphere, fossil fuel combustion, biomass burning, and biofuel combustion, all scaled to a total flux of 1 Pg C for each continental region. The black boxes represent the receptor regions used for the transit time analysis shown in Fig. 15.

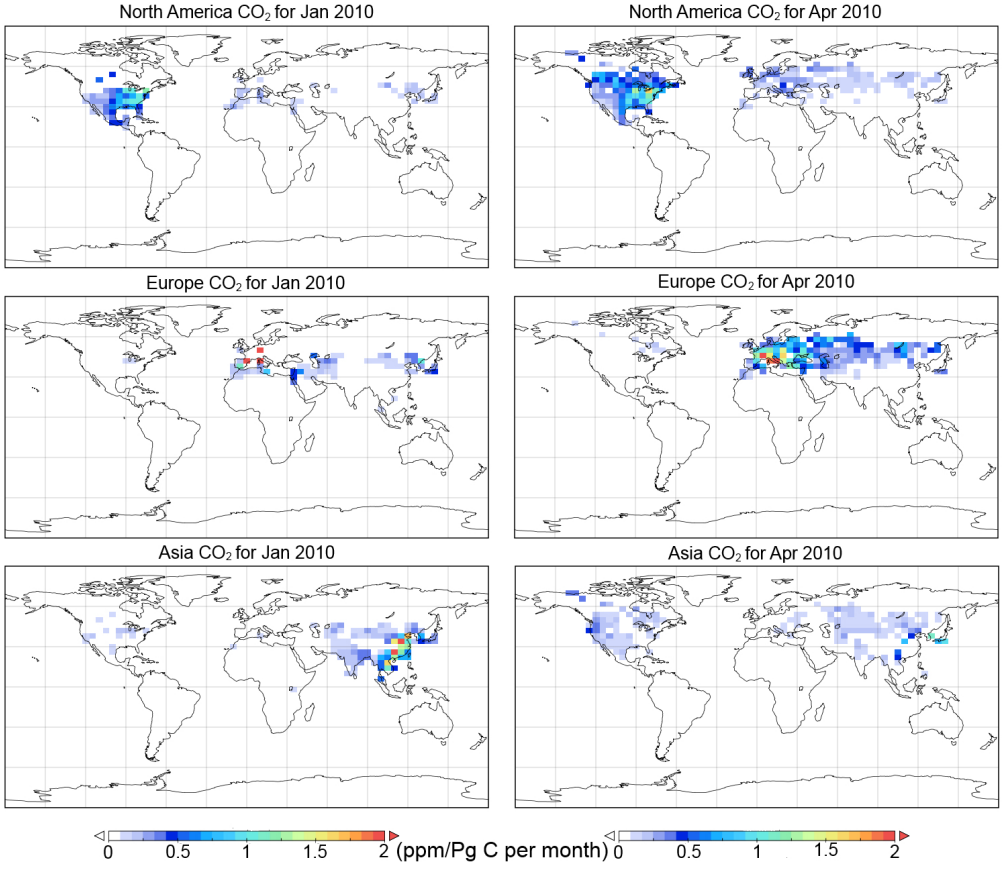

Fig. 13. Sensitivity of modeled XCO_2-to-CO_2 fluxes (ppm/Pg C per month) for North America (top row), Europe (middle row), and Asia (bottom row). Shown are the sensitivities of XCO_2 in January (left column) and April (right column) to fluxes in January and April, respectively.

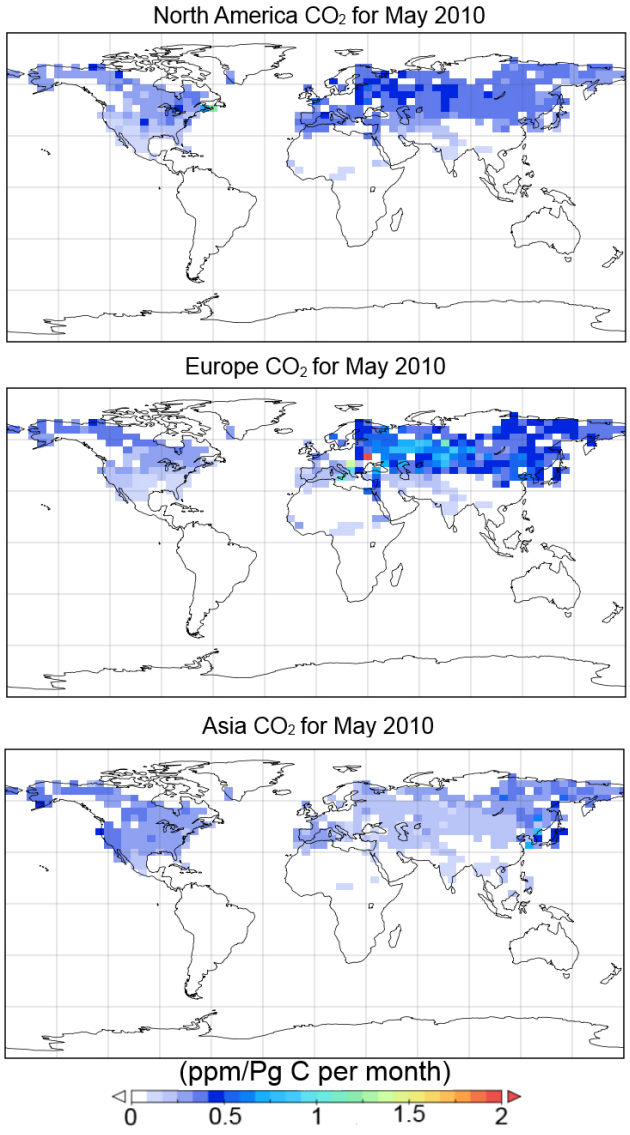

Fig. 14. Sensitivity of modeled XCO_2-to-CO_2 fluxes (ppm/Pg C per month) for North America (top row), Europe (middle row), and Asia (bottom row). Shown are the sensitivities of XCO_2 in May to fluxes in April.

each region within one day to simulate the release of each tracer that is a delta function in time, producing a tracer distribution that is analogous to an age spectrum (Hall and Plumb, 1994; Holzer and Hall, 2008). Fig. 15 shows the transit times to the middle troposphere over the receptor regions in Fig. 12 for June 2010 conditions. To reduce the influence of the changing synoptic conditions in June on the distribution of the transit times, we averaged the distribution of transit times obtained from pulse releases of the tracers on 1, 10, and 20 June 2010. The distributions of transit times shown in Fig. 15 are consistent with those shown by Holzer and Hall (2008). As expected, over each continental region, transport of CO_2 from the boundary layer to the middle troposphere peaks on the timescale of a few days. Fig. 15 shows the rapid transport of North American air across the Atlantic. Within 10–20 days, North American CO_2 is transported across to Europe and Siberia. This suggests that, in the context of the inversion, on timescales of one to two weeks, North American flux estimates can be influenced by XCO_2 observations across North America and Eurasia. In contrast, over eastern Asia and the Pacific, the North American signal is well mixed into the background.

Examination of Fig. 15 reveals that the transport of European CO_2 out of Europe and Siberia is sufficiently long that outside of these regions the European signal is also well mixed into the background. This suggests that European flux estimates should be influenced mainly by observations over Europe and Siberia, on timescales of about one or two weeks, respectively. As a result, the European flux estimates should be sensitive mainly to biases in the XCO_2 data over Eurasia, whereas North American flux estimates should be sensitive to regional biases in the data over North America as well as over Eurasia. This greater influence of long-range transport on the North American fluxes suggests that North American flux estimates should be more sensitive to model transport errors than European flux estimates. However, the actual impact on the estimated fluxes will depend on the relative magnitudes of the North American and European fluxes.

The timescale for transport across the Pacific Ocean is longer than for transport across the Atlantic Ocean; however, Fig. 15 shows that the Asian signal remains above the background across the Pacific and over North America. Despite this influence of long-range transport on the Asian fluxes, our inversion exhibited low sensitivity to Asian CO_2 fluxes due to the absence of ocean observations and the limited GOSAT observational coverage over eastern Asia, as a result of cloud cover. This suggests that incorporating ocean observations over the midlatitude and northern Pacific should produce greater constraints on the Asian fluxes.

5 Conclusions

We have conducted inversion analyses using three different sets of the NASA ACOS GOSAT XCO_2 b2.9 and b2.10 data to quantify regional sources and sinks of atmospheric CO_2. We found that the seasonal variations of the inferred global fluxes were consistent across the three XCO_2 inversions. The inversions significantly increased the uptake estimate in the northern extratropics during growing season, suggesting that the a priori fluxes may have underestimated the seasonal cycle amplitude in the northern extratropics. The a posteriori CO_2 was in better agreement with independent TCCON, surface flask, and HIPPO aircraft observations. On regional spatial scales, we found that the flux estimates were sensitive to the treatment of the residual bias in the GOSAT XCO_2 data. The largest differences obtained were for temperate North America and temperate South America, for which the largest

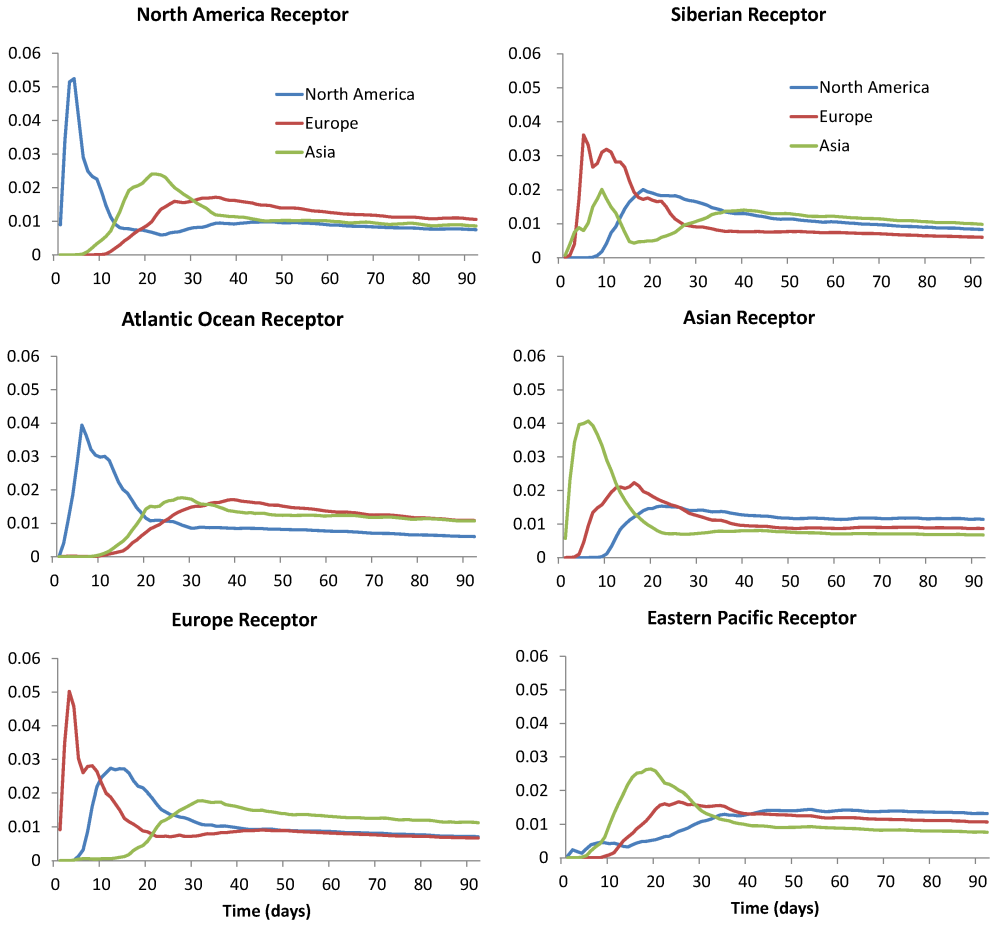

Fig. 15. Transit times (in days) of North American, European, and Asian CO_2 to the middle troposphere of the receptor regions shown in Fig. 12. The transit times were estimated based on three pulse releases of CO_2 of 1 Pg C on 1, 10, and 20 June from each continental region. The resulting tracer distributions were normalized such that the integral of the tracer abundance, averaged over the receptor region, for the 90-day period of the simulation is unity.

spread between the inversions was 1.02 and 0.96 Pg C, respectively. In the case of temperate North America, one inversion suggested a strong source (RUN_A), whereas the second and third inversion produced a weak (RUN_B) and strong sink (RUN_C), respectively. However, inversion of the surface flask data produced an even stronger sink for temperate North America than was inferred from the GOSAT data. We found that the flux estimates from boreal Eurasia, temperate Eurasia, and Europe were generally consistent across the three XCO_2 inversions. Comparison of the a posteriori flux estimates with the MPI-BGC eddy-covariance-flux-based product showed that the inferred European fluxes were consistent with the eddy covariance flux product, whereas the North American fluxes were offset by ∼1 month and a weaker sink.

The XCO_2 inversions produced the largest uncertainty reduction on the flux estimates for South America and Africa, with the greatest uncertainty reduction on the flux estimates for tropical South America. In the northern extratropics, the largest uncertainty reduction was for the temperate North American flux estimates, which our sensitivity analysis suggests could be due to the fact that North American flux estimates are sensitive to observations over Eurasia on timescales of one to two weeks as a result of the long-range transport of CO_2 from North America. In contrast, European flux estimates are sensitive to observations on the Eurasian continent on timescales of less than a week. We note that the analysis presented here was an initial attempt at understanding the inversion results in the context of the transit times. It suggests that the North American flux estimates are more strongly influenced by long-range transport and should, therefore, be more sensitive to regionally varying biases in the observations and to model transport errors. In addition, the low sensitivity of the European flux estimates to observations outside of Eurasia could explain why the inferred European flux estimates are more robust across the three different XCO_2 data sets. However, there is clear need for more detailed analyses to better characterize the sensitivity of the

inferred regional flux estimates to the transport pathways and transit times associated with long-range transport of the continental CO_2 signals.

We found that the GOSAT observational coverage is a challenge for the inversion. The greater sensitivity to North American fluxes than European and Asia fluxes, for example, is due to the lack of observations over Eurasia in winter and over eastern and southern Asia in summer. Since the observations over Eurasia are restricted to summer, it is unclear how reliable the European flux estimates are, despite the fact that they are robust across the three XCO_2 inversions. Increased wintertime observational coverage in Eurasia is critical for better quantifying the seasonal variation in the extratropical sources and sinks of CO_2. The use of M-gain GOSAT data over North Africa would also provide additional constraints on European flux estimates. A particular concern is the low sensitivity to temperate Asian fluxes in the inversion. During the growing season, the data density is low over temperate Asia as a result of cloud cover from the Asian monsoon. The use of ocean observations over the Pacific would help capture the Asian outflow and better quantify the Asian fluxes. Similarly, observations over the North Atlantic would provide useful information on North American CO_2 fluxes. The ocean glint data from GOSAT could be useful in this context, but these data are mainly in the tropics and subtropics. Incorporating the thermal infrared (TIR) GOSAT CO_2 retrievals with the XCO_2 data could better capture the continental outflow and provide greater constraints on the Asian, North American, and tropical fluxes, from regions such as the Amazon, where persistent cloud cover is a challenge for the GOSAT retrievals.

Although the global flux estimates inferred in the different inversion analyses presented here were robust, the regional flux estimates were less reliable. In our analyses, we focused on fixed regions, as defined by TransCom, to facilitate comparison with previous inversion analyses in the literature. However, the actual regional scales on which the inversion analyses can constrain the flux estimates will depend on the observational coverage, the observational error, the specified a priori flux errors, and the changing atmospheric transport patterns. An objective approach is clearly needed to determine the minimum spatial scales at which the fluxes can be reliably quantified. There is also a critical need for additional independent data to better evaluate the inferred fluxes. Despite the large spread in the flux estimates obtained for regions such as temperate North America, tropical South America, and temperate South America, we found that the different inversion analyses reproduced well the independent atmospheric CO_2 data and were similar in their agreement with the data (with mean differences typically less than 0.5 ppm). This raises the issue as to how we should employ the existing data sets, and what additional observations are needed, to provide a more stringent evaluation of the inferred flux estimates.

Acknowledgements. This work was funded by the NASA Atmospheric CO_2 Observations from Space (ACOS) program (grant number NNX10AT42G), the Canadian Space Agency, and the Natural Sciences and Engineering Research Council of Canada. Work at the Jet Propulsion Laboratory, California Institute of Technology, was carried out under contract to NASA. D. Henze and N. Bousserez were also supported by the NASA Carbon Monitoring System (CMS) flux plot project. US funding for TCCON comes from NASA's Carbon Cycle Program, grant number NNX11AG01G, the Orbiting Carbon Observatory Program, and the DOE/ARM Program. The European TCCON groups involved in this study acknowledge financial support by the EU infrastructure project InGOS. The University of Bremen acknowledges financial support of the Bialystok and Orleans TCCON sites from the Senate of Bremen and EU projects IMECC, GEOmon and InGOS, as well as maintenance and logistical work provided by AeroMeteo Service (Bialystok) and the RAMCES team at LSCE (Gif-sur-Yvette, France) and additional operational funding from the National Institute for Environmental Studies (NIES, Japan). TCCON measurements at Eureka were made by the Canadian Network for Detection of Atmospheric Composition Change (CANDAC) with additional support from the Canadian Space Agency. We thank NOAA-ESRL for making their CO_2 surface measurements publicly available. Anonymous referees provided constructive comments that greatly improved this paper.

Edited by: C. Gerbig

References

Andres, R. J., Gregg, J. S., Losey, L., Marland, G., and Boden, T. A.: Monthly, global emissions of carbon dioxide from fossil fuel consumption, Tellus B, 63, 309–327, doi:10.1111/j.1600-0889.2011.00530.x, 2011.

Baker, D. F., Doney, S. C., and Schimel, D. S.: Variational data assimilation for atmospheric CO_2, Tellus B, 58, 359–365, doi:10.1111/j.1600-0889.2006.00218.x, 2006a.

Baker, D. F., Law, R. M., Gurney, K. R., Rayner, P., Peylin, P., Denning, A. S., Bousquet, P., Bruhwiler, L., Chen, Y. H., Ciais, P., Fung, I. Y., Heimann, M., John, J., Maki, T., Maksyutov, S., Masarie, K., Prather, M., Pak, B., Taguchi, S., and Zhu, Z.: TransCom 3 inversion intercomparison: Impact of transport model errors on the interannual variability of regional CO_2 fluxes, 1988–2003, Global Biogeochem. Cy., 20, GB1002, doi:10.1029/2004gb002439, 2006b.

Baldocchi, D.: TURNER REVIEW No. 15.'Breathing' of the terrestrial biosphere: lessons learned from a global network of carbon dioxide flux measurement systems, Aust. J. Bot., 56, 1–26, doi:10.1071/BT07151, 2008.

Baldocchi, D., Falge, E., Gu, L., Olson, R., Hollinger, D., Running, S., Anthoni, P., Bernhofer, C., Davis, K., Evans, R., Fuentes, J., Goldstein, A., Katul, G., Law, B., Lee, X., Malhi, Y., Meyers, T., Munger, W., Oechel, W., Paw, K. T., Pilegaard, K., Schmid, H. P., Valentini, R., Verma, S., Vesala, T., Wilson, K., and Wofsy, S.: FLUXNET: A New Tool to Study the Temporal and Spatial Variability of Ecosystem–Scale Carbon Dioxide, Water Vapor, and Energy Flux Densities, B. Am. Meteorol. Soc., 82, 2415–2434, doi:10.1175/1520-0477(2001)082<2415:FANTTS>2.3.CO;2, 2001.

Basu, S., Houweling, S., Peters, W., Sweeney, C., Machida, T., Maksyutov, S., Patra, P. K., Saito, R., Chevallier, F., Niwa, Y., Matsueda, H., and Sawa, Y.: The seasonal cycle amplitude of total column CO_2: Factors behind the model-observation mismatch, J. Geophys. Res., 116, D23306, doi:10.1029/2011jd016124, 2011.

Basu, S., Guerlet, S., Butz, A., Houweling, S., Hasekamp, O., Aben, I., Krummel, P., Steele, P., Langenfelds, R., Torn, M., Biraud, S., Stephens, B., Andrews, A., and Worthy, D.: Global CO_2 fluxes estimated from GOSAT retrievals of total column CO_2, Atmos. Chem. Phys. Discuss., 13, 4535-4600, doi:10.5194/acpd-13-4535-2013, 2013.

Blunden, J., Arndt, D. S., and Baringer, M. O.: State of the Climate in 2010, B. Am. Meteorol. Soc., 92, S1–S236, doi:10.1175/1520-0477-92.6.s1, 2011.

Bruhwiler, L. M. P., Michalak, A. M., and Tans, P. P.: Spatial and temporal resolution of carbon flux estimates for 1983–2002, Biogeosciences, 8, 1309–1331, doi:10.5194/bg-8-1309-2011, 2011.

Canadell, J. G., Le Quéré, C., Raupach, M. R., Field, C. B., Buitenhuis, E. T., Ciais, P., Conway, T. J., Gillett, N. P., Houghton, R. A., and Marland, G.: Contributions to accelerating atmospheric CO_2 growth from economic activity, carbon intensity, and efficiency of natural sinks, Proc. Natl. Acad. Sci., 104, 18866–18870, doi:10.1073/pnas.0702737104, 2007.

Chen, J. M., Liu, J., Cihlar, J., and Goulden, M. L.: Daily canopy photosynthesis model through temporal and spatial scaling for remote sensing applications, Ecol. Model., 124, 99–119, 1999.

Chen, J. M., Mo, G., Pisek, J., Liu, J., Deng, F., Ishizawa, M., and Chan, D.: Effects of foliage clumping on the estimation of global terrestrial gross primary productivity, Global Biogeochem. Cy., 26, doi:10.1029/2010GB003996, 2012.

Chevallier, F., Bréon, F.-M., and Rayner, P. J.: Contribution of the Orbiting Carbon Observatory to the estimation of CO_2 sources and sinks: Theoretical study in a variational data assimilation framework, J. Geophys. Res., 112, D09307, doi:10.1029/2006JD007375, 2007.

Chevallier, F., Maksyutov, S., Bousquet, P., Bréon, F.-M., Saito, R., Yoshida, Y., and Yokota, T.: On the accuracy of the CO_2 surface fluxes to be estimated from the GOSAT observations, Geophysical Research Letters, 36, L19807, doi:10.1029/2009GL040108, 2009.

Conway, T. J. and Tans, P.: NOAA/ESRL (www.esrl.noaa.gov/gmd/ccgg/trends/) 2012.

Conway, T. J., Lang, P. M., and Masarie, K. A.: Atmospheric Carbon Dioxide Dry Air Mole Fractions from the NOAA ESRL Carbon Cycle Cooperative Global Air Sampling Network, 1968-2010, Version: 2011-10-14, ftp://ftp.cmdl.noaa.gov/ccg/co2/flask/event/ 2011.

Corbett, J. J.: Considering alternative input parameters in an activity-based ship fuel consumption and emissions model: Reply to comment by Øyvind Endresen et al. on "Updated emissions from ocean shipping", J. Geophys. Res., 109, D23303, doi:10.1029/2004jd005030, 2004.

Corbett, J. J. and Koehler, H. W.: Updated emissions from ocean shipping, J. Geophys. Res., 108, 4650–4666, doi:10.1029/2003jd003751, 2003.

Deng, F. and Chen, J. M.: Recent global CO_2 flux inferred from atmospheric CO_2 observations and its regional analyses, Biogeosciences, 8, 3263–3281, doi:10.5194/bg-8-3263-2011, 2011.

Deng, F., Chen, J. M., Plummer, S., Chen, M., and Pisek, J.: Algorithm for global leaf area index retrieval using satellite imagery, IEEE Trans. Geosci. Remote Sens., 44, 2219–2229, doi:10.1109/tgrs.2006.872100, 2006.

Deng, F., Chen, J. M., Ishizawa, M., Yuen, C.-W., Mo, G., Higuchi, K., Chan, D., and Maksyutov, S.: Global monthly CO_2 flux inversion with a focus over North America, Tellus B, 59, 179–190, doi:10.1111/j.1600-0889.2006.00235.x, 2007.

Deutscher, N. M., Griffith, D. W. T., Bryant, G. W., Wennberg, P. O., Toon, G. C., Washenfelder, R. A., Keppel-Aleks, G., Wunch, D., Yavin, Y., Allen, N. T., Blavier, J. F., Jiménez, R., Daube, B. C., Bright, A. V., Matross, D. M., Wofsy, S. C., and Park, S.: Total column CO_2 measurements at Darwin, Australia – site description and calibration against in situ aircraft profiles, Atmos. Meas. Tech., 3, 947–958, doi:10.5194/amt-3-947-2010, 2010.

Endresen, Ø., Sørgård, E., Bakke, J., and Isaksen, I. S. A.: Substantiation of a lower estimate for the bunker inventory: Comment on "Updated emissions from ocean shipping" by James J. Corbett and Horst W. Koehler, J. Geophys. Res., 109, D23302, doi:10.1029/2004jd004853, 2004.

Endresen, Ø., Sørgård, E., Behrens, H. L., Brett, P. O., and Isaksen, I. S. A.: A historical reconstruction of ships' fuel consumption and emissions, J. Geophys. Res., 112, D12301, doi:10.1029/2006JD007630, 2007.

Enting, I. G., Trudinger, C. M., and Francey, R. J.: A synthesis inversion of the concentration and δ^{13} C of atmospheric CO_2, Tellus B, 47, 35–52, 1995.

Fan, S., Gloor, M., Mahlman, J., Pacala, S., Sarmiento, J., Takahashi, T., and Tans, P.: A Large Terrestrial Carbon Sink in North America Implied by Atmospheric and Oceanic Carbon Dioxide Data and Models, Science, 282, 442–446, doi:10.1126/science.282.5388.442, 1998.

Gurney, K. R., Law, R. M., Denning, A. S., Rayner, P. J., Baker, D., Bousquet, P., Bruhwiler, L., Chen, Y.-H., Ciais, P., Fan, S., Fung, I. Y., Gloor, M., Heimann, M., Higuchi, K., John, J., Maki, T., Maksyutov, S., Masarie, K., Peylin, P., Prather, M., Pak, B. C., Randerson, J., Sarmiento, J., Taguchi, S., Takahashi, T., and Yuen, C.-W.: Towards robust regional estimates of CO_2 sources and sinks using atmospheric transport models, Nature, 415, 626–630, 2002.

Gurney, K. R., Law, R. M., Denning, A. S., Rayner, P. J., Pak, B. C., Baker, D., Bousquet, P., Bruhwiler, L., Chen, Y.-H., Ciais, P., Fung, I. Y., Heimann, M., John, J., Maki, T., Maksyutov, S., Peylin, P., Prather, M., and Taguchi, S.: Transcom 3 inversion intercomparison: Model mean results for the estimation of seasonal carbon sources and sinks, Global Biogeochem. Cy., 18, GB1010, doi:10.1029/2003GB002111, 2004.

Hall, T. M. and Plumb, R. A.: Age as a diagnostic of stratospheric transport, J. Geophys. Res.: Atmospheres, 99, 1059–1070, doi:10.1029/93JD03192, 1994.

Heald, C. L., Jacob, D. J., Jones, D. B. A., Palmer, P. I., Logan, J. A., Streets, D. G., Sachse, G. W., Gille, J. C., Hoffman, R. N., and Nehrkorn, T.: Comparative inverse analysis of satellite (MOPITT) and aircraft (TRACE-P) observations to estimate Asian sources of carbon monoxide, J. Geophys. Res. Atmos., 109, D23306, doi:10.1029/2004jd005185, 2004.

Henze, D. K., Hakami, A., and Seinfeld, J. H.: Development of the adjoint of GEOS-Chem, Atmos. Chem. Phys., 7, 2413–2433, doi:10.5194/acp-7-2413-2007, 2007.

Henze, D. K., Seinfeld, J. H., and Shindell, D. T.: Inverse modeling and mapping US air quality influences of inorganic PM2.5 precursor emissions using the adjoint of GEOS-Chem, Atmos. Chem. Phys., 9, 5877–5903, doi:10.5194/acp-9-5877-2009, 2009.

Holzer, M. and Hall, T. M.: Tropospheric transport climate partitioned by surface origin and transit time, J. Geophys. Res. Atmos., 113, D08104, doi:10.1029/2007JD009115, 2008.

Houweling, S., Breon, F. M., Aben, I., Rödenbeck, C., Gloor, M., Heimann, M., and Ciais, P.: Inverse modeling of CO_2 sources and sinks using satellite data: a synthetic inter-comparison of measurement techniques and their performance as a function of space and time, Atmos. Chem. Phys., 4, 523–538, doi:10.5194/acp-4-523-2004, 2004.

Jiang, Z., Jones, D. B. A., Kopacz, M., Liu, J., Henze, D. K., and Heald, C.: Quantifying the impact of model errors on top-down estimates of carbon monoxide emissions using satellite observations, J. Geophys. Res., 116, D15306, doi:10.1029/2010jd015282, 2011.

Jones, C., McConnell, C., Coleman, K., Cox, P., Falloon, P., Jenkinson, D., and Powlson, D.: Global climate change and soil carbon stocks; predictions from two contrasting models for the turnover of organic carbon in soil, Global Change Biol., 11, 154–166, 2005.

Jung, M., Reichstein, M., and Bondeau, A.: Towards global empirical upscaling of FLUXNET eddy covariance observations: validation of a model tree ensemble approach using a biosphere model, Biogeosciences, 6, 2001–2013, doi:10.5194/bg-6-2001-2009, 2009.

Jung, M., Reichstein, M., Margolis, H. A., Cescatti, A., Richardson, A. D., Arain, M. A., Arneth, A., Bernhofer, C., Bonal, D., Chen, J., Gianelle, D., Gobron, N., Kiely, G., Kutsch, W., Lasslop, G., Law, B. E., Lindroth, A., Merbold, L., Montagnani, L., Moors, E. J., Papale, D., Sottocornola, M., Vaccari, F., and Williams, C.: Global patterns of land-atmosphere fluxes of carbon dioxide, latent heat, and sensible heat derived from eddy covariance, satellite, and meteorological observations, J. Geophys. Res.: Biogeosciences, 116, G00J07, doi:10.1029/2010JG001566, 2011.

Kalnay, E., Kanamitsu, M., Kistler, R., Collins, W., Deaven, D., Gandin, L., Iredell, M., Saha, S., White, G., Woollen, J., Zhu, Y., Leetmaa, A., Reynolds, R., Chelliah, M., Ebisuzaki, W., Higgins, W., Janowiak, J., Mo, K. C., Ropelewski, C., Wang, J., Jenne, R., and Joseph, D.: The NCEP/NCAR 40-Year Reanalysis Project, B. Am. Meteorol. Soc., 77, 437–471, doi:10.1175/1520-0477(1996)077<0437:TNYRP>2.0.CO;2, 1996.

Kim, B. Y., Fleming, G. G., Lee, J. J., Waitz, I. A., Clarke, J.-P., Balasubramanian, S., Malwitz, A., Klima, K., Locke, M., Holsclaw, C. A., Maurice, L. Q., and Gupta, M. L.: System for assessing Aviation's Global Emissions (SAGE), Part 1: Model description and inventory results, Trans. Res. D Trans. Environ., 12, 325–346, doi:10.1016/j.trd.2007.03.007, 2007.

Kopacz, M., Jacob, D. J., Henze, D. K., Heald, C. L., Streets, D. G., and Zhang, Q.: Comparison of adjoint and analytical Bayesian inversion methods for constraining Asian sources of carbon monoxide using satellite (MOPITT) measurements of CO columns, J. Geophys. Res., 114, D04305, doi:10.1029/2007jd009264, 2009.

Kopacz, M., Mauzerall, D. L., Wang, J., Leibensperger, E. M., Henze, D. K., and Singh, K.: Origin and radiative forcing of black carbon transported to the Himalayas and Tibetan Plateau, Atmos. Chem. Phys., 11, 2837–2852, doi:10.5194/acp-11-2837-2011, 2011.

Kuze, A., Suto, H., Nakajima, M., and Hamazaki, T.: Thermal and near infrared sensor for carbon observation Fourier-transform spectrometer on the Greenhouse Gases Observing Satellite for greenhouse gases monitoring, Appl. Opt., 48, 6716–6733, 2009.

Law, R. M., Chen, Y.-H., Gurney, K. R., and Modellers, T.: TransCom 3 CO_2 inversion intercomparison: 2. Sensitivity of annual mean results to data choices, Tellus B, 55, 580–595, 2003.

Li, Q., Jacob, D. J., Bey, I., Palmer, P. I., Duncan, B. N., Field, B. D., Martin, R. V., Fiore, A. M., Yantosca, R. M., Parrish, D. D., Simmonds, P. G., and Oltmans, S. J.: Transatlantic transport of pollution and its effects on surface ozone in Europe and North America, J. Geophys. Res.: Atmospheres, 107, ACH 4-1–ACH 4-21, doi:10.1029/2001JD001422, 2002.

Liu, D. C. and Nocedal, J.: On the limited memory BFGS method for large scale optimization, Math/ Prog., 45, 503-528, doi:10.1007/bf01589116, 1989.

Maksyutov, S., Takagi, H., Valsala, V. K., Saito, M., Oda, T., Saeki, T., Belikov, D. A., Saito, R., Ito, A., Yoshida, Y., Morino, I., Uchino, O., Andres, R. J., and Yokota, T.: Regional CO_2 flux estimates for 2009–2010 based on GOSAT and ground-based CO_2 observations, Atmos. Chem. Phys., 13, 9351–9373, doi:10.5194/acp-13-9351-2013, 2013.

Marland, G.: Uncertainties in Accounting for CO_2 From Fossil Fuels, J. Ind. Ecol., 12, 136–139, 2008.

Messerschmidt, J., Geibel, M. C., Blumenstock, T., Chen, H., Deutscher, N. M., Engel, A., Feist, D. G., Gerbig, C., Gisi, M., Hase, F., Katrynski, K., Kolle, O., Lavrič, J. V., Notholt, J., Palm, M., Ramonet, M., Rettinger, M., Schmidt, M., Sussmann, R., Toon, G. C., Truong, F., Warneke, T., Wennberg, P. O., Wunch, D., and Xueref-Remy, I.: Calibration of TCCON column-averaged CO_2: the first aircraft campaign over European TCCON sites, Atmos. Chem. Phys., 11, 10765–10777, doi:10.5194/acp-11-10765-2011, 2011.

Michalak, A. M., Hirsch, A., Bruhwiler, L., Gurney, K. R., Peters, W., and Tans, P. P.: Maximum likelihood estimation of covariance parameters for Bayesian atmospheric trace gas surface flux inversions, J. Geophys. Res., 110, D24107, doi:10.1029/2005jd005970, 2005.

Müller, J. F. and Stavrakou, T.: Inversion of CO and NOx emissions using the adjoint of the IMAGES model, Atmos. Chem. Phys., 5, 1157–1186, doi:10.5194/acp-5-1157-2005, 2005.

Nassar, R., Jones, D. B. A., Suntharalingam, P., Chen, J. M., Andres, R. J., Wecht, K. J., Yantosca, R. M., Kulawik, S. S., Bowman, K. W., Worden, J. R., Machida, T., and Matsueda, H.: Modeling global atmospheric CO_2 with improved emission inventories and CO_2 production from the oxidation of other carbon species, Geosci. Model Dev., 3, 689–716, doi:10.5194/gmd-3-689-2010, 2010.

Nassar, R., Jones, D. B. A., Kulawik, S. S., Worden, J. R., Bowman, K. W., Andres, R. J., Suntharalingam, P., Chen, J. M., Brenninkmeijer, C. A. M., Schuck, T. J., Conway, T. J., and Worthy, D. E.: Inverse modeling of CO_2 sources and sinks using satellite

observations of CO_2 from TES and surface flask measurements, Atmos. Chem. Phys., 11, 6029–6047, doi:10.5194/acp-11-6029-2011, 2011.

O'Dell, C. W., Connor, B., Bösch, H., O'Brien, D., Frankenberg, C., Castano, R., Christi, M., Eldering, D., Fisher, B., Gunson, M., McDuffie, J., Miller, C. E., Natraj, V., Oyafuso, F., Polonsky, I., Smyth, M., Taylor, T., Toon, G. C., Wennberg, P. O., and Wunch, D.: The ACOS CO_2 retrieval algorithm – Part 1: Description and validation against synthetic observations, Atmos. Meas. Tech., 5, 99-121, doi:10.5194/amt-5-99-2012, 2012.

Palmer, P. I., Jacob, D. J., Fiore, A. M., Martin, R. V., Chance, K., and Kurosu, T. P.: Mapping isoprene emissions over North America using formaldehyde column observations from space, J. Geophys. Res. Atmos., 108, 4180–4192, doi:10.1029/2002jd002153, 2003.

Park, B. C. and Prather, M. J.: CO_2 source inversions using satellite observations of the upper troposphere, Geophysical Research Letters, 28, 4571–4574, doi:10.1029/2001GL013604, 2001.

Patra, P. K., Maksyutov, S., Ishizawa, M., Nakazawa, T., Takahashi, T., and Ukita, J.: Interannual and decadal changes in the sea-air CO_2 flux from atmospheric CO_2 inverse modeling, Global Biogeochem. Cy., 19, GB4013, doi:10.1029/2004GB002257, 2005.

Peters, W., Jacobson, A. R., Sweeney, C., Andrews, A. E., Conway, T. J., Masarie, K., Miller, J. B., Bruhwiler, L. M. P., Pétron, G., Hirsch, A. I., Worthy, D. E. J., van der Werf, G. R., Randerson, J. T., Wennberg, P. O., Krol, M. C., and Tans, P. P.: An atmospheric perspective on North American carbon dioxide exchange: CarbonTracker, Proc. Natl. Acad. Sci., 104, 18925–18930, doi:10.1073/pnas.0708986104, 2007.

Peters, W., Krol, M. C., Van Der Werf, G. R., Houweling, S., Jones, C. D., Hughes, J., Schaefer, K., Masarie, K. A., Jacobson, A. R., Miller, J. B., Cho, C. H., Ramonet, M., Schmidt, M., Ciattaglia, L., Apadula, F., Heltai, D., Meinhardt, F., Di Sarra, A. G., Piacentino, S., Sferlazzo, D., Aalto, T., Hatakka, J., Ström, J., Haszpra, L., Meijer, H. A. J., Van Der Laan, S., Neubert, R. E. M., Jordan, A., Rodó, X., MorguÍ, J. A., Vermeulen, A. T., Popa, E., Rozanski, K., Zimnoch, M., Manning, A. C., Leuenberger, M., Uglietti, C., Dolman, A. J., Ciais, P., Heimann, M., and Tans, P. P.: Seven years of recent European net terrestrial carbon dioxide exchange constrained by atmospheric observations, Global Change Biol., 16, 1317–1337, doi:10.1111/j.1365-2486.2009.02078.x, 2010.

Peylin, P., Baker, D., Sarmiento, J., Ciais, P., and Bousquet, P.: Influence of transport uncertainty on annual mean and seasonal inversions of atmospheric CO_2 data, J. Geophys. Res., 107, 4385–4409, doi:10.1029/2001JD000857, 2002.

Randerson, J. T., Hoffman, F. M., Thornton, P. E., Mahowald, N. M., Lindsay, K., Lee, Y.-H., Nevison, C. D., Doney, S. C., Bonan, G., StÖCkli, R., Covey, C., Running, S. W., and Fung, I. Y.: Systematic assessment of terrestrial biogeochemistry in coupled climate-carbon models, Global Change Biol., 15, 2462–2484, doi:10.1111/j.1365-2486.2009.01912.x, 2009.

Rayner, P. J. and O'Brien, D. M.: The utility of remotely sensed CO_2 concentration data in surface source inversions, Geophysical Research Letters, 28, 175-178, doi:10.1029/2000GL011912, 2001.

Rayner, P. J., Enting, I. G., Francey, R. J., and Langenfelds, R.: Reconstructing the recent carbon cycle from atmospheric CO_2, $\delta^{13}C$ and O_2/N_2 observations, Tellus B, 51, 213–232, doi:10.1034/j.1600-0889.1999.t01-1-00008.x, 1999.

Rayner, P. J., Law, R. M., Allison, C. E., Francey, R. J., Trudinger, C. M., and Pickett-Heaps, C.: Interannual variability of the global carbon cycle (1992-2005) inferred by inversion of atmospheric CO_2 and $\delta_{13}CO_2$ measurements, Global Biogeochem. Cy., 22, GB3008, doi:10.1029/2007GB003068, 2008.

Rödenbeck, C., Houweling, S., Gloor, M., and Heimann, M.: CO_2 flux history 1982-2001 inferred from atmospheric data using a global inversion of atmospheric transport, Atmos. Chem. Phys., 3, 1919–1964, doi:10.5194/acp-3-1919-2003, 2003.

Stephens, B. B., Gurney, K. R., Tans, P. P., Sweeney, C., Peters, W., Bruhwiler, L., Ciais, P., Ramonet, M., Bousquet, P., Nakazawa, T., Aoki, S., Machida, T., Inoue, G., Vinnichenko, N., Lloyd, J., Jordan, A., Heimann, M., Shibistova, O., Langenfelds, R. L., Steele, L. P., Francey, R. J., and Denning, A. S.: Weak Northern and Strong Tropical Land Carbon Uptake from Vertical Profiles of Atmospheric CO_2, Science, 316, 1732–1735, doi:10.1126/science.1137004, 2007.

Takagi, H., Saeki, T., Oda, T., Saito, M., Valsala, V., Belikov, D., Saito, R., Yoshida, Y., Morino, I., Uchino, O., Andres, R. J., Yokota, T., and Maksyutov, S.: On the Benefit of GOSAT Observations to the Estimation of Regional CO_2 Fluxes, Sola, 7, 161–164, doi:10.2151/sola.2011-041, 2011.

Takahashi, T., Sutherland, S. C., Wanninkhof, R., Sweeney, C., Feely, R. A., Chipman, D. W., Hales, B., Friederich, G., Chavez, F., Sabine, C., Watson, A., Bakker, D. C. E., Schuster, U., Metzl, N., Yoshikawa-Inoue, H., Ishii, M., Midorikawa, T., Nojiri, Y., Körtzinger, A., Steinhoff, T., Hoppema, M., Olafsson, J., Arnarson, T. S., Tilbrook, B., Johannessen, T., Olsen, A., Bellerby, R., Wong, C. S., Delille, B., Bates, N. R., and de Baar, H. J. W.: Climatological mean and decadal change in surface ocean pCO_2, and net sea-air CO_2 flux over the global oceans, Deep Sea Res. II: Topical Stud. Oceanogr., 56, 554–577, 2009.

Tarantola, A.: Inverse Problem Theory and Methods for Model Parameter Estimation, Soc. Industr. App.l Math., Philadelphia, PA, USA, 2004.

Thompson, J. E., Hayes, P. L., Jimenez, J. L., Adachi, K., Zhang, X., Liu, J., Weber, R. J., and Buseck, P. R.: Aerosol optical properties at Pasadena, CA during CalNex 2010, Atmospheric Environment, 55, 190–200, doi:10.1016/j.atmosenv.2012.03.011, 2012.

van der Werf, G. R., Randerson, J. T., Giglio, L., Collatz, G. J., Mu, M., Kasibhatla, P. S., Morton, D. C., DeFries, R. S., Jin, Y., and van Leeuwen, T. T.: Global fire emissions and the contribution of deforestation, savanna, forest, agricultural, and peat fires (1997–2009), Atmos. Chem. Phys., 10, 11707–11735, doi:10.5194/acp-10-11707-2010, 2010.

Washenfelder, R. A., Toon, G. C., Blavier, J. F., Yang, Z., Allen, N. T., Wennberg, P. O., Vay, S. A., Matross, D. M., and Daube, B. C.: Carbon dioxide column abundances at the Wisconsin Tall Tower site, J. Geophys. Res., 111, D22305, doi:10.1029/2006jd007154, 2006.

Wilkerson, J. T., Jacobson, M. Z., Malwitz, A., Balasubramanian, S., Wayson, R., Fleming, G., Naiman, A. D., and Lele, S. K.: Analysis of emission data from global commercial aviation: 2004 and 2006, Atmos. Chem. Phys., 10, 6391–6408, doi:10.5194/acp-10-6391-2010, 2010.

Wofsy, S. C., Team, H. S., Cooperating, M., and Satellite, T.: HIAPER Pole-to-Pole Observations (HIPPO): fine-grained, global-

scale measurements of climatically important atmospheric gases and aerosols, Phil. Trans. A Math. Phys. Eng. Sci., 369, 2073–2086, doi:10.1098/rsta.2010.0313, 2011.

Wofsy, S. C., Daube, B. C., Jimenez, R., Kort, E., Pittman, J. V., Park, S., Commane, R., Xiang, B., Santoni, G., Jacob, D., Fisher, J., Pickett-Heaps, C., Wang, H., Wecht, K., Wang, Q.-Q., Stephens, B. B., Shertz, S., Watt, A. S., Romashkin, P., Campos, T., Haggerty, J., Cooper, W. A., Rogers, D., Beaton, S., Hendershot, R., Elkins, J. W., Fahey, D. W., Gao, R. S., Moore, F., Montzka, S. A., Schwarz, J. P., Perring, A. E., Hurst, D., Miller, B. R., Sweeney, C., Oltmans, S., Nance, D., Hintsa, E., Dutton, G., Watts, L. A., Spackman, J. R., Rosenlof, K. H., Ray, E. A., Hall, B., Zondlo, M. A., Diao, M., Keeling, R., Bent, J., Atlas, E. L., Lueb, R., and Mahoney, M. J.: HIPPO Merged 10-second Meteorology, Atmospheric Chemistry, Aerosol Data (R_20121129), Carbon Dioxide Information Analysis Center, Oak Ridge National Laboratory, Oak Ridge, Tennessee, USA, 2012.

Wunch, D., Toon, G. C., Wennberg, P. O., Wofsy, S. C., Stephens, B. B., Fischer, M. L., Uchino, O., Abshire, J. B., Bernath, P., Biraud, S. C., Blavier, J. F. L., Boone, C., Bowman, K. P., Browell, E. V., Campos, T., Connor, B. J., Daube, B. C., Deutscher, N. M., Diao, M., Elkins, J. W., Gerbig, C., Gottlieb, E., Griffith, D. W. T., Hurst, D. F., Jiménez, R., Keppel-Aleks, G., Kort, E. A., Macatangay, R., Machida, T., Matsueda, H., Moore, F., Morino, I., Park, S., Robinson, J., Roehl, C. M., Sawa, Y., Sherlock, V., Sweeney, C., Tanaka, T., and Zondlo, M. A.: Calibration of the Total Carbon Column Observing Network using aircraft profile data, Atmos. Meas. Tech., 3, 1351–1362, doi:10.5194/amt-3-1351-2010, 2010.

Wunch, D., Wennberg, P. O., Toon, G. C., Connor, B. J., Fisher, B., Osterman, G. B., Frankenberg, C., Mandrake, L., O'Dell, C., Ahonen, P., Biraud, S. C., Castano, R., Cressie, N., Crisp, D., Deutscher, N. M., Eldering, A., Fisher, M. L., Griffith, D. W. T., Gunson, M., Heikkinen, P., Keppel-Aleks, G., Kyrö, E., Lindenmaier, R., Macatangay, R., Mendonca, J., Messerschmidt, J., Miller, C. E., Morino, I., Notholt, J., Oyafuso, F. A., Rettinger, M., Robinson, J., Roehl, C. M., Salawitch, R. J., Sherlock, V., Strong, K., Sussmann, R., Tanaka, T., Thompson, D. R., Uchino, O., Warneke, T., and Wofsy, S. C.: A method for evaluating bias in global measurements of CO_2 total columns from space, Atmos. Chem. Phys., 11, 12317–12337, doi:10.5194/acp-11-12317-2011, 2011.

Yevich, R., and Logan, J. A.: An assessment of biofuel use and burning of agricultural waste in the developing world, Global Biogeochem. Cy., 17, 1095–1134, doi:10.1029/2002GB001952, 2003.

Zhao, C. L. and Tans, P. P.: Estimating uncertainty of the WMO mole fraction scale for carbon dioxide in air, J. Geophys. Res., 111, D08S09, doi:10.1029/2005JD006003, 2006.